
Time-resolved spectroscopy and photometry of an M dwarf flare star YZ Canis Minoris with OISTER and TESS: Blue asymmetry in $H\alpha$ line during the non-white light flare

**Hiroyuki MAEHARA¹, Yuta NOTSU^{2,3}, Kousuke NAMEKATA⁴, Satoshi
HONDA⁵, Adam F. KOWALSKI^{2,3,6}, Noriyuki KATOH^{5,7}, Tomohito OHSHIMA⁵,
Kota IIDA⁸, Motoki OEDA⁸, Katsuhiko L. MURATA⁸, Masayuki
YAMANAKA^{9,10}, Kengo TAKAGI¹¹, Mahito SASADA⁹, Hiroshi AKITAYA⁹, Kai
IKUTA⁴, Soshi OKAMOTO⁴, Daisaku NOGAMI⁴ and Kazunari SHIBATA¹²**

¹Subaru Telescope Okayama Branch Office, National Astronomical Observatory of Japan,
National Institutes of Natural Sciences, 3037-5 Honjo, Kamogata, Asakuchi, Okayama
719-0232, Japan

²Laboratory for Atmospheric and Space Physics, University of Colorado Boulder, 3665
Discovery Drive, Boulder, CO 80303, USA

³National Solar Observatory, University of Colorado Boulder, 3665 Discovery Drive, Boulder,
CO 80303, USA.

⁴Department of Astronomy, Kyoto University, Kitashirakawa-Oiwake-cho, Sakyo, Kyoto
606-8502, Japan

⁵Nishi-Harima Astronomical Observatory, Center for Astronomy, University of Hyogo, Sayo,
Sayo, Hyogo 679-5313, Japan

⁶Department of Astrophysical and Planetary Sciences, University of Colorado Boulder, 2000
Colorado Ave, Boulder, CO 80305, USA.

⁷Graduate School of Human Development and Environment, Kobe University, 3-11
Tsurukabuto, Nada-ku, Kobe, Hyogo 657-8501, Japan

⁸Department of Physics, Tokyo Institute of Technology, 2-12-1 Ookayama, Meguro-ku, Tokyo
152-8551, Japan

⁹Hiroshima Astrophysical Science Center, Hiroshima University, Higashi-Hiroshima,
Hiroshima 739-8526, Japan

¹⁰Okayama Observatory, Kyoto University, 3037-5 Honjo, Kamogata, Asakuchi, Okayama
719-0232, Japan

¹¹Department of Physical Science, Hiroshima University, Kagamiyama 1-3-1,
Higashi-Hiroshima 739-8526, Japan

¹²Kwasan Observatory, Yamashina, Kyoto 607-8471, Japan

*E-mail: hiroyuki.maehara@nao.ac.jp

Received ; Accepted

Abstract

In this paper, we present the results from spectroscopic and photometric observations of the M-type flare star YZ CMi in the framework of the Optical and Infrared Synergetic Telescopes for Education and Research (OISTER) collaborations during the Transiting Exoplanet Survey Satellite (TESS) observation period. We detected 145 white-light flares from the TESS light curve and 4 H α flares from the OISTER observations performed between 2019-01-16 and 2019-01-18. Among them, 3 H α flares were associated with white-light flares. However, one of them did not show clear brightening in continuum; during this flare, the H α line exhibited blue-asymmetry which has lasted for ~ 60 min. The line of sight velocity of the blue-shifted component is $-80 - -100$ km s $^{-1}$. This suggests that there can be upward flows of chromospheric cool plasma even without detectable red/NIR continuum brightening. By assuming that the blue-asymmetry in H α line was caused by a prominence eruption on YZ CMi, we estimated the mass and kinetic energy of the upward-moving material to be $10^{16} - 10^{18}$ g and $10^{29.5} - 10^{31.5}$ erg, respectively. The estimated mass is comparable to expectations from the empirical relation between the flare X-ray energy and mass of upward-moving material for stellar flares and solar CMEs. In contrast, the estimated kinetic energy for the non-white-light flare on YZ CMi is roughly 2 orders of magnitude smaller than that expected from the relation between flare X-ray energy and kinetic energy for solar CMEs. This could be understood by the difference in the velocity between CMEs and prominence eruptions.

Key words: stars: activity, stars: flare, stars: rotation

1 Introduction

Solar flares are sudden and energetic explosions in the solar atmosphere around sunspots. Flares are observed in all wavelength bands from radio to high-energy gamma-rays. They are thought to be the rapid releases of magnetic energy through magnetic reconnection in the solar corona (e.g. Shibata & Magara 2011 and referenes theirin). Part of the energy released by the magnetic reconnection is transported from the reconnection site into the chromosphere via thermal conduction and high-energy particles, which causes heating, produces line emission (e.g., $H\alpha$), and can even produce hard X-ray and optical continuum emission. This intense heating of chromospheric plasma is thought to cause the upward flow of plasma called chromospheric evaporation (Fisher et al. 1985).

Similar periods of rapid increases and slow decays of intensity in radio, optical and X-ray bands are also observed on various types of stars, and they are called stellar flares. In particular, it is known that young stellar objects, close binary systems and M-type main sequence stars (dMe stars) exhibit frequent and energetic flares (e.g., Shibata & Yokoyama 2002; Gershberg 2005; Reid & Hawley 2005; Benz & Güdel 2010; Hawley et al. 2014; Linsky 2019; Namekata et al. 2020b). Because of the similarity in observational properties between stellar flares and solar flares (e.g., Nuepert effect in solar/stellar flares; Neupert 1968; Dennis & Zarro 1993; Hawley et al. 1995; Guedel et al. 1996), they are considered to be caused by the same physical processes (i.e., plasma heating by accelerated particles and evaporation). Many spectroscopic studies of superflares have been carried out in order to understand the dynamics of plasma during flares and radiation mechanisms of flares. Various spectroscopic observations of solar flares have shown that chromospheric lines (e.g., $H\alpha$, Ca II, Mg II) often exhibit asymmetric line profiles during flares. Red asymmetries (enhancement of the red wing) have been frequently observed during the impulsive phase of the flares (e.g. Švestka et al. 1962; Ichimoto & Kurokawa 1984; Canfield et al. 1990; Shoji & Kurokawa 1995; Berlicki 2007; Kuridze et al. 2015; Kowalski et al. 2017; Graham et al. 2020). This is thought to be caused by the chromospheric condensation, which is the downward flow of cool plasma in the chromosphere. Blue asymmetries (enhancement of the blue wing) have also been observed mainly in the early phase of flares (e.g., Švestka et al. 1962; Canfield et al. 1990; Heinzel et al. 1994b; Kuridze et al. 2016; Tei et al. 2018; Huang et al. 2019). It is suggested that blue asymmetry is caused by an upflow of cool plasma, which is lifted up by expanding hot plasma owing to the deep penetration of non-thermal electrons into the chromosphere during a flare (Tei et al. 2018; Huang et al. 2019). However, the detailed origin of this blue asymmetries are still controversial.

Similar line asymmetries in chromospheric lines (especially $H\alpha$) have been observed during stellar flares. In addition to red asymmetries (e.g., Houdebine et al. 1993), various blue asymmetries have been widely observed (e.g., Houdebine et al. 1990; Gunn et al. 1994; Fuhrmeister et al. 2008; Vida et al. 2016; Honda et al. 2018; Muheki et al. 2020). Vida et al. 2016 reported several $H\alpha$ flares on the M4 dwarf V374 Peg showing blue asymmetries with the line-of-sight velocity of $-200 - -400 \text{ km s}^{-1}$. They also found that red-wing enhancements in the $H\alpha$ line were observed after blue asymmetries, which suggest the erupted cool plasma falling back on the stellar surface. Honda et al. 2018 reported a long duration $H\alpha$ flare on the M4.5 dwarf EV Lac. During this flare, a blue asymmetry in the $H\alpha$ line with the dopper velocity of $\sim -100 \text{ km s}^{-1}$ has been observed for > 2 hours. Since we cannot obtain the spatially resolved information for stellar flares, the line of sight motions of cool plasma such as coronal rains, surges, and filament/prominence eruptions may also cause red/blue asymmetries. For example, if the cool plasma is launched upward and seen above the limb, the emission can cause blue- or red-shifted enhancements of the $H\alpha$ line (e.g. Odert et al. 2020). As observed on the Sun, such eruptions (surges and filament/prominence eruptions) can evolve into CMEs (coronal mass ejections) if the erupted plasma is accelerated and the velocity exceeds the escape velocity (e.g., Gopalswamy et al. 2003, Shibata & Magara 2011, and reference therein).

Other studies have suggested that blue asymmetries in chromospheric lines may be due to stellar mass ejections. Vida et al. (2019) reported a statistical analysis of 478 stellar events with asymmetries in Balmer lines of M-dwarfs, which were found from more than 5500 “snapshot” spectra (cf. Similar events were also reported from other snapshot data in Fuhrmeister et al. 2018). The velocity and mass of the possible ejected materials estimated from the blue- or red-shifted excess in Balmer lines range from $100 - 300 \text{ km s}^{-1}$ and $10^{15} - 10^{18} \text{ g}$, respectively. Moschou et al. (2019) presented the correlations between mass/kinetic energy of CMEs and X-ray energy of associated flares on various types of stars. They found that estimated stellar flare CME masses are consistent with the trends extrapolated from solar events but kinematic energies are roughly two orders of magnitude smaller than expected. It is important to understand the properties of stellar CMEs in order to evaluate effects of stellar activities not only on the mass- and angular momentum loss of the star (e.g. Osten & Wolk 2015; Odert et al. 2017, Cranmer 2017), but also on the habitability (e.g., loss of atmosphere, atmospheric chemistry, climate, radiation dose) of exoplanets (e.g., Lammer et al. 2007, Linsky 2019, Segura et al. 2010, Tilley et al. 2019, Scheucher et al. 2018, Airapetian et al. 2020, Yamashiki et al. 2019). However, our understanding of asymmetries in chromospheric lines and their connections with stellar flares/CMEs is still limited by the low number of samples observed in time-resolved

spectroscopy simultaneously with high-precision photometry.

In order to investigate the connection between the blue/red asymmetries in H α line and properties of flares, we conducted photometric and spectroscopic observations of an active M dwarf, YZ CMi, during the Transiting Exoplanet Survey Satellite (TESS; Ricker et al. 2015) observation window (sector 7: from 2019-01-07 to 2019-02-01). In this paper, we report on results from the statistical analysis of flares on YZ CMi from TESS light curve and photometric and spectroscopic observations in the framework of the Optical and Infrared Synergetic Telescopes for Education and Research (OISTER; Yamanaka et al. in prep.). The details of our observations and analysis are described in section 2. We present the properties of detected flares from TESS and OISTER observations in section 3. In section 4, we discuss (1) the differences between H α flares with and without white-light flares, (2) blue asymmetry observed during the H α flare without a white-light flare, (3) the rotational modulations observed in continuum and H α emission line, and (4) the statistical properties of flare duration.

2 Data and methods

2.1 Target star: YZ CMi

YZ CMi (= Gl 285 = Ross 882) is a well-known 11 mag M4.5Ve flare star, whose distance from the Earth is about 5.99 pc (Gaia Collaboration et al. 2018). Flares on YZ CMi were first discovered at optical wavelengths by van Maanen (1945) and were later detected at radio wavelengths (Lovell 1969; Spangler et al. 1974) and X-ray wavelengths (Grindlay & Heise 1975). Frequent stellar flares have been observed on YZ CMi in several wavelength ranges (Lacy et al. 1976; Mitra-Kraev et al. 2005; Kowalski et al. 2013), and in particular, a large superflare whose U-band energy is larger than 10^{34} erg is reported in Kowalski et al. (2010). Zeeman broadening measurements suggest the existence of strong magnetic fields on the stellar surface (e.g., Johns-Krull & Valenti 2000; Reiners & Basri 2007). According to ZeemanDoppler Imaging observation, the visible pole of YZ CMi is covered by a strong spot with the radial magnetic field strength of up to 3 kG (Morin et al. 2008).

2.2 Flare detection from the TESS light curve

We analyzed the TESS Sector 7 PDC-SAP light curve (Vanderspek et al. 2018; Fausnaugh et al. 2019) of YZ CMi retrieved from the MAST Portal site¹. In order to detect small flares, we first removed non-flare signals such as long-term trend and rotational brightness variations from

¹ <https://mast.stsci.edu/portal/Mashup/Clients/Mast/Portal.html>

the light curve and then searched for flares. Since there is a data gap between BJD 2458503.04 and 2458504.71 in the TESS light curve (Fig. 1), we divided the whole TESS light curve into two subsets (BJD 2458491.64 – 2458503.04 and BJD 2458504.71 – 2458516.09), and analyzed each light curve subset separately. First we removed some of the large flares from the light curve beforehand since large flares with long flare duration affect the long-term light curve fitting process. The initial flare detection was performed with the same method used in our previous studies (Maehara et al. 2012; Shibayama et al. 2013). The excluded data points in the light curve were interpolated by using “`interpolate.Akima1DInterpolator`” in the Python Scipy package. After removing flares and interpolation of the removed data points, we extracted the long-term trend and rotational variations by using the 5th-order Bessel filter in the SciPy signal module. We used the cut-off frequency of 0.2 d^{-1} in this process. Then we removed the extracted signal from light curves. We selected the data points satisfying the following conditions as the flare candidates: (1) the residual brightness of the data point is higher than the upper 10 percent of the residual light curve, (2) at least two consecutive data points exceed the flare detection threshold, (3) decay time is longer than rise time. Finally we checked all the light curves of flare candidates by eye and eliminated the misidentified candidates. The total number of the automatically selected flare candidates is 194 and the number of confirmed flares is 145. A table of the flares identified in TESS (with peak time, flare amplitude normalized by the average stellar brightness, equivalent duration (the model-independent energy in units of seconds; Gershberg 1972), bolometric energy of flare, and flare e-folding time) is provided in Supplementary Data (Table_S1.csv).

2.3 OISTER observations

We conducted the coordinated observing campaign of YZ CMi on 2019-01-16, 17, and 18 in the framework of OISETR collaboration. The log of the observation is summarised in Table 1.

Simultaneous multi-color (g -, R_C -, and I_C -bands ²) photometry was carried out by using the MITSuME 50-cm telescope at Okayama, Japan (Kotani et al. 2005). All the images taken by MITSuME were dark subtracted and flat-fielded by using IRAF ³ in the standard manner before the photometry was performed. We carried out aperture photometry of YZ CMi and several surrounding stars on each image with the APPHOT package in IRAF. We used a

² The effective wavelength (λ_0) and bandwidth (FWHM) are $\lambda_0 = 4770 \text{ \AA}$ and $\text{FWHM} = 1380 \text{ \AA}$ for g -band (Fukugita et al. 1996), $\lambda_0 = 6407 \text{ \AA}$ and $\text{FWHM} = 1580 \text{ \AA}$ for R_C -band (Bessell 2005), $\lambda_0 = 7980 \text{ \AA}$ and $\text{FWHM} = 1540 \text{ \AA}$ for I_C -band (Bessell 2005), respectively.

³ IRAF is distributed by the National Optical Astronomy Observatories, which are operated by the Association of Universities for Research in Astronomy, Inc., under cooperate agreement with the National Science Foundation.

nearby K III star HD 62525 ($V = 8.072$, $B - V = 0.810$; magnitude and color are taken from the AAVSO Variable Star Plotter (VSP)⁴) as a local standard star for photometry. The constancy of brightness of the comparison star during our observation was checked by using TYC 183-2106-1 ($V = 10.661$, $B - V = 0.458$; taken from VSP).

We also performed time-resolved low ($R = \lambda/\Delta\lambda \sim 400$) and medium ($R = \lambda/\Delta\lambda \sim 10000$) resolution spectroscopy by using the HOWPol (Kawabata et al. 2008) mounted on the 1.5-m Kanata telescope at Higashi Hiroshima Observatory, Hiroshima University and the MALLS (Medium And Low-dispersion Long-slit Spectrograph; Ozaki & Tokimasa 2005) mounted on the 2.0-m Nayuta telescope at Nishi-Harima Astronomical Observatory, University of Hyogo, respectively. After the standard image reduction processes such as dark-subtraction and flat-fielding, we analyzed the data by using the TWODSPEC and ONEDSPEC packages in IRAF. For the spectra taken with Kanata/HOWPol, the wavelength calibration was performed by using O I and Hg sky glow lines. For the spectra taken with Nayuta/MALLS, we used an Fe/Ne/Ar lamp for wavelength calibration. In addition to the standard wavelength calibration procedure by using the comparison frames, we corrected the instrumental drift of the spectrum in the wavelength dimension over time by using the atmospheric absorption features. We also applied corrections for the barycentric velocity and the absolute stellar radial velocity (26.495 km s⁻¹; Soubiran et al. 2018) to the wavelength of spectra.

2.4 APO observations

In this paper, we used Apache Point Observatory (APO) data only for rotational modulations discussed in Section 4.3. The detailed results including flares from the APO observations will be presented in our forthcoming paper (Notsu et al. in prep.). The log of the observation is also summarised in Table 1. We carried out g -band photometry with the Flarecam instrument (Hilton 2011) of 0.5-m Astrophysical Research Consortium Small Aperture Telescope (ARCSAT) at APO on 2019-01-26, 27, and 28 (UT). Dark subtraction and flat-fielding were performed by using PyRAF⁵ software in the standard manner before the photometry. Aperture photometry was performed by using AstroimageJ⁶ (Collins et al. 2017). We used nearby stars as the magnitude reference. Spectroscopic observations were carried out by using the ARC Echelle Spectrograph (ARCES; Wang et al. 2003) attached to the ARC 3.5 m telescope at

⁴ <https://www.aavso.org/apps/vsp/>

⁵ PyRAF is part of the stscipython package of astronomical data analysis tools and is a product of the Science Software Branch at the Space Telescope Science Institute.

⁶ <https://www.astro.louisville.edu/software/astroimagej/>

Table 1. Log of OISTER and APO observations.

Telescope/Instrument	Start-End (UT)	Exp. time (sec)	Number of data
MITSuME 0.5m	2019-01-16.625 - 16.793	5	590 (<i>g</i>), 608 (<i>R_C</i>), 610 (<i>I_C</i>)
(<i>g</i> , <i>R_C</i> , <i>I_C</i> -band)	17.713 - 17.786	5	123 (<i>g</i>), 124 (<i>R_C</i>), 124 (<i>I_C</i>)
Okayama, Japan	18.623 - 18.793	5	853 (<i>g</i>), 891 (<i>R_C</i>), 895 (<i>I_C</i>)
Kanata 1.5m/HOWPol	16.625 - 16.816	60	224
(4000-9000Å; $\lambda/\Delta\lambda \sim 400$)	17.667 - 17.740	60	77
Hiroshima, Japan	18.639 - 18.792	60	186
Nayuta 2m/MALLS	16.604 - 16.801	250	54
(6350-6800Å; $\lambda/\Delta\lambda \sim 10000$)	18.629 - 18.793	250	51
Hyogo, Japan			
ARCSAT 0.5m/flarecam	26.131 - 26.423	4, 15, 30*	310 (<i>g</i>)
(<i>g</i> -band)	27.113 - 27.418	4	138 (<i>g</i>)
New Mexico, United States	28.108 - 28.402	4, 6, 12, 20*	155 (<i>g</i>)
ARC 3.5m/ARCES	26.118 - 26.420	600, 900*	28
(3800-10000Å; $\lambda/\Delta\lambda \sim 32000$)	27.110 - 27.421	300	60
New Mexico, United States	28.112 - 28.413	300, 600*	54

* We adjusted the exposure time as needed since the sky was covered by a thin layer of clouds.

APO on 2019-01-26, 27, and 28 (UT). The wavelength resolution ($R = \lambda/\Delta\lambda$) is ~ 32000 , and the spectral coverage is 3800-10000 Å. After the standard image reduction procedures such as bias subtraction, flat-fielding, and scattered light subtraction, we analyzed the data by using the ECHELLE package in IRAF and PyRAF software. We used a Th/Ar lamp for wavelength calibration. We also applied the heliocentric radial velocity correction by using the ECHELLE package. These analysis methods of spectroscopic data are the same as Notsu et al. (2019). The $H\alpha$ equivalent width values are measured from these spectra.

3 Results

3.1 TESS observations

Fig. 1 shows the light curve of YZ CMi observed with TESS. We can clearly see a sinusoidal modulation with a period of ~ 2.8 days and many flares. We applied the Phase Dispersion Minimization(PDM) method (Stellingwerf 1978) to the flare-removed light curve and found that the best-estimated period of the sinusoidal modulation is 2.774 ± 0.0014 days, which is consistent with the rotation period of YZ CMi (Pettersen et al. 1983; Morin et al. 2008).

After removing the rotational light variations, we detected 145 flares in the TESS light curve. As shown in Fig. 1, the largest flare observed with TESS shows a flare peak amplitude of

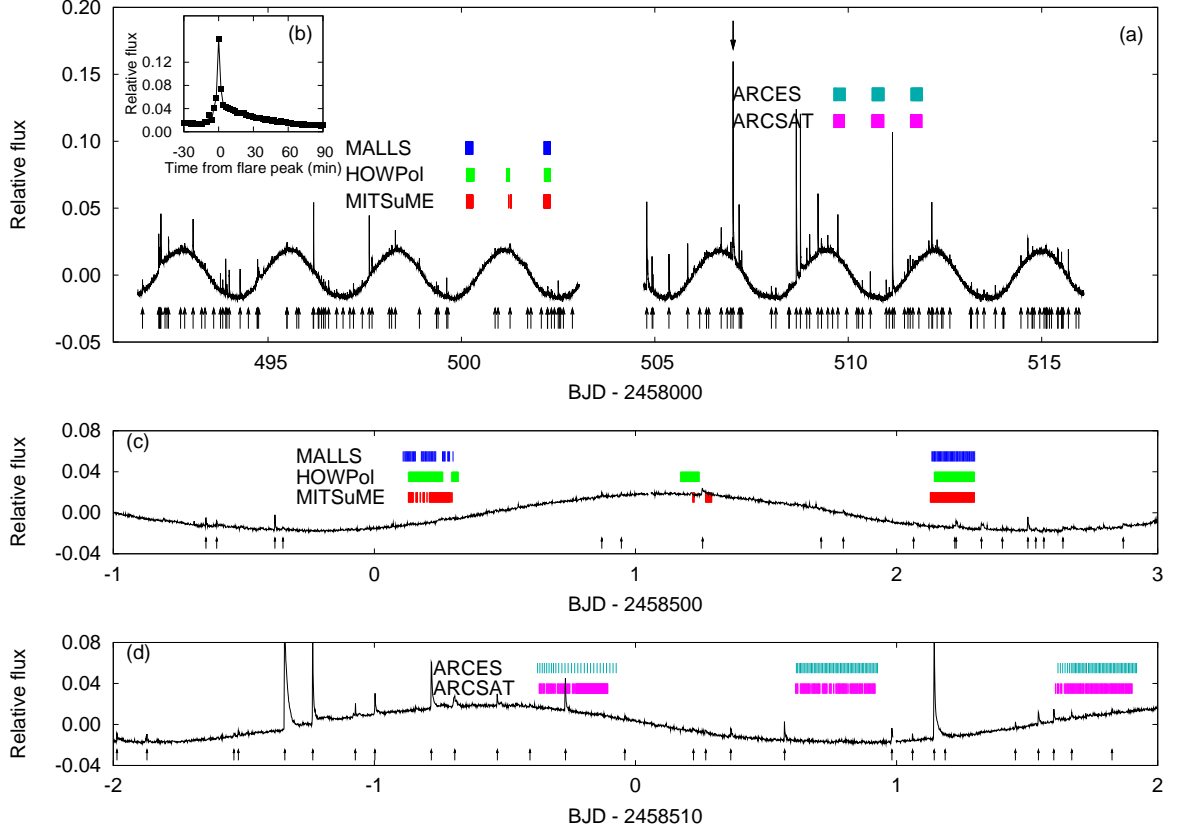


Fig. 1. (a) Light curve of YZ CMi observed with TESS, covering the times of OISTER and APO observations. The horizontal and vertical axes represent the observation time in Barycentric Julian Date (BJD) and relative flux normalized by the average flux. The red, green and blue bars in panels (a) and (c) indicate the times of observations by MITSuME (g -, R_C -, and I_C -band photometry), HOWPol (low-resolution spectroscopy) and MALLS (medium-resolution spectroscopy), respectively. The magenta and cyan bars in (a) and (c) indicate g -band photometry with ARCSAT and high-resolution spectroscopy by ARCRES at APO. Up-arrows below the light curve indicate the peak times of flares detected by our flare detection method. (b) Light curve of the largest flare on YZ CMi observed with TESS during the TESS Sector 7 (denoted by a down-arrow in panel a). The horizontal axis is the time from the flare peak ($T_0(\text{BJD}) = 2458507.0233$). (c) Same as (a) but for the light curve around OISTER observations. (d) Same as (a) but for the light curve around APO observations.

$\sim 14\%$ relative to the average stellar brightness and a duration of ~ 70 min. We estimated the bolometric energy released by flares under the assumption that the spectral energy distribution of the flare component is similar to blackbody radiation with an effective temperature of 10000 K (e.g., Hawley & Pettersen 1991; Hawley & Fisher 1992 for flares on M dwarfs). We also assumed that the effective temperature and radius of YZ CMi are 3300 K and $0.3 R_\odot$ (Gaidos & Mann 2014; Newton et al. 2015; Houdebine et al. 2016). The amplitude of a flare ($\Delta F/F$) on YZ CMi observed in TESS band ($6000 - 10000 \text{ \AA}$; centered on the traditional Cousins I_C -band, $\lambda_0 \sim 8000 \text{ \AA}$; Ricker et al. 2015) can be written as

$$\frac{\Delta F}{F} = \frac{A_{\text{flare}}}{A_{1/2\text{star}}} \frac{\int B(T_{\text{flare}}, \lambda) S(\lambda) d\lambda}{\int B(T_{\text{star}}, \lambda) S(\lambda) d\lambda}, \quad (1)$$

where $A_{\text{flare}}/A_{1/2\text{star}}$ is the fraction of flare emitting area normalized by the effective area of stellar hemisphere, T_{flare} and T_{star} are the effective temperature of flare component and that of star, λ is the wavelength, $B(T, \lambda)$ is the Planck function, and $S(\lambda)$ is the spectral response function of TESS detector. The bolometric luminosity of flare (L_{flare}) can be estimated by

$$L_{\text{flare}} = \sigma T_{\text{flare}}^4 A_{\text{flare}}, \quad (2)$$

where σ is the StefanBoltzmann constant. For the flare with $\Delta F/F = 1$, $A_{\text{flare}}/A_{1/2\text{star}}$ would be ~ 0.018 which corresponds to the flare bolometric luminosity of $\sim 2.4 \times 10^{31}$ erg s $^{-1}$. It should be noted that the fraction of bolometric flux for the blackbody radiation with an effective temperature of 10000 K which falls within the TESS bandpass is only ~ 20 %. According to Kowalski et al. (2013), some flares exhibit large Balmer jump. The near-ultraviolet (NUV) continuum for such flares differs from the blackbody and the blackbody approximation would underestimate the NUV continuum flare flux by a factor of two (Kowalski et al. 2019). This suggests that the estimated bolometric flare energy may have an uncertainty by a factor of 2-3. The bolometric energy released by observed flares ranges from 7×10^{30} erg to 3×10^{33} erg. Fig. 2 shows the cumulative flare frequency distribution (CFFD; panel a) and flare frequency distribution (FFD; dN/dE , panel b) as a function of flare energy (E), respectively. The FFD can be fitted by a power-law distribution ($dN/dE \propto E^{-\alpha}$) with a power-law index of $\alpha = 1.75 \pm 0.04$ in the bolometric flare energy range of 10^{32} to 10^{34} erg. The power-law slope from YZ CMi's FFD is similar to those of other M dwarfs (e.g., Lacy et al. 1976; Shakhovskaia 1989; Audard et al. 2000; Hawley et al. 2014; Silverberg et al. 2016) and the Sun (e.g., Crosby et al. 1993; Aschwanden et al. 2000).

3.2 OISTER photometry and spectroscopy

During the OISTER observing campaign, we detected 4 H α flares from time-resolved spectroscopy as shown in Fig. 3, 4, and 5. On January 16, 2019, an H α flare with a peak timing of 2458500.26 (“flare A”) was detected (Fig. 3 (a) and (b)). During this flare, H α and H β equivalent widths ⁷ changed by -2 \AA and -7 \AA , respectively. In addition to the enhancement of the Balmer emission lines, the continuum brightness observed with TESS also increased by 0.3%. We estimated the luminosity of the flare component by using the distance to YZ CMi (5.99 pc; Gaia Collaboration et al. 2018), the flux-calibrated quiescent spectra (Kowalski et al.

⁷ The equivalent width of a spectral line is defined as a area of the line on a plot of the continuum-normalized intensity as a function of wavelength. In this paper, since a negative value of the equivalent width indicates line emission, a decrease (negative change) of equivalent width indicates an increase of emission line flux.

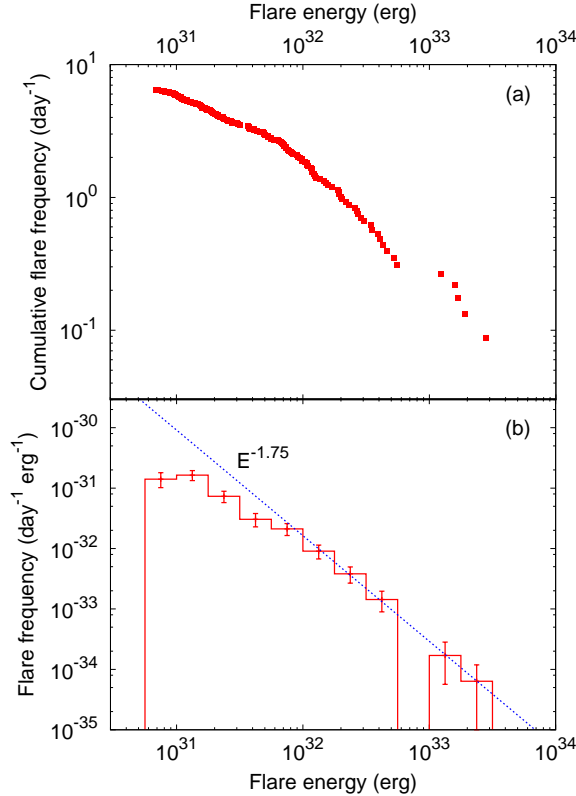


Fig. 2. (a) Cumulative flare frequency distribution as a function of flare energy. The horizontal axis is the bolometric energy released by flares. The vertical axis represents the cumulative flare frequency, the number of flares with the flare energy larger than a give value per day. Please note that we cannot detect the flares whose occurrence frequency is much less than $\sim 4.5 \times 10^{-2} \text{ day}^{-1}$ since the total observation time is ~ 22 days. (b) Flare frequency distribution as a function of flare energy. The horizontal axis represents the flare frequency normalized by the bin width. Dotted line represents a power-law fit to the data in the flare energy range from 10^{32} erg to 10^{34} erg. The power-law index estimated from the fit is -1.75 ± 0.04 .

2013), g -, R_C -, and I_C -band magnitudes. The peak luminosity of this flare in the $H\alpha$ and $H\beta$ lines is $1.2 \times 10^{27} \text{ erg s}^{-1}$ and $0.9 \times 10^{27} \text{ erg s}^{-1}$, respectively (Fig. 3 (c)). The peak luminosity of this flare in the TESS band is estimated to be $1.5 \times 10^{28} \text{ erg s}^{-1}$ (Fig. 3 (d)).

During the short observing run on January 17, 2019, a small and short-duration $H\alpha$ flare was detected at BJD 2458501.2125 (“flare B”). The equivalent width of the $H\beta$ emission line and continuum flux observed with TESS also increased during this flare (Fig. 4). The amplitude of this flare in $H\alpha$, $H\beta$ and TESS band are -1 \AA , -4 \AA , and 0.2% , respectively. These values correspond to the flare peak luminosity of $0.8 \times 10^{27} \text{ erg s}^{-1}$ ($H\alpha$), $\sim 1.2 \times 10^{27} \text{ erg s}^{-1}$ ($H\beta$), and $0.9 \times 10^{28} \text{ erg s}^{-1}$ (TESS band), respectively.

We detected 2 $H\alpha$ flares during the OISTER observation on January 18, 2019. These two flares show different properties: the flare at BJD 2458502.177 (“flare C”) shows slow rise and slow decay, while the double-peaked flare at BJD 2458502.228 (“flare D”) shows rapid rise

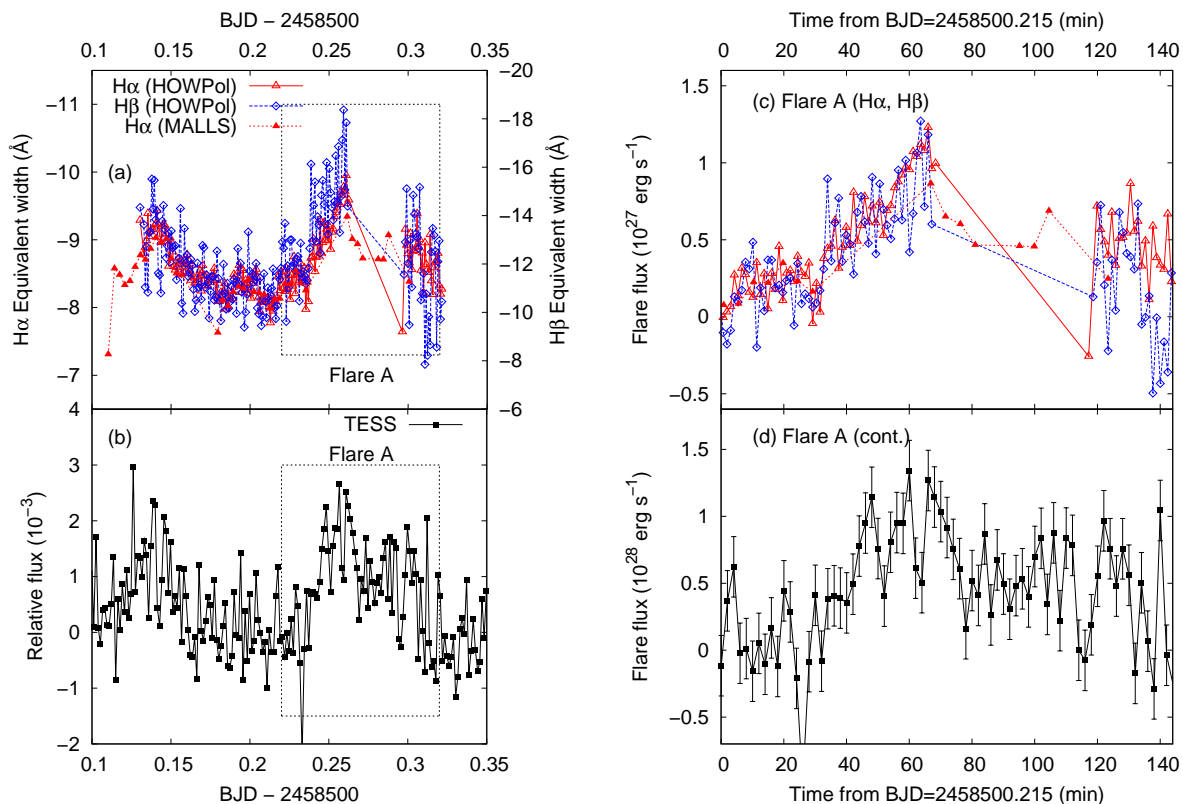


Fig. 3. (a) H α , H β light curve of YZ CMi on January 16. The horizontal axis represents the observation time in Barycentric Julian Date (BJD). Left and right vertical axes represent equivalent widths of the H α and H β lines, respectively (values are negative for emission lines). Open and filled triangles indicate the equivalent width of the H α line measured from spectra obtained with Kanata/HOWPol and Nayuta/MALLS, respectively. Open diamonds represent the equivalent width of the H β line measured from spectra obtained with Kanata/HOWPol. (b) TESS light curve of YZ CMi during the OISTER observations on January 16. The vertical axis represents the relative flux normalized by the stellar average flux. (c) Enlarged H α and H β light curves of flare A. The horizontal and vertical axis represent the time from BJD 2458500.215 and the flare component's luminosity. Open triangles and open diamonds indicate the luminosities of the flare component in the H α and H β lines. The flux calibration for the H α and H β lines were performed by using the quiescent spectra taken from Kowalski et al. (2013), g - and R_C -band magnitudes. (d) Same as panel (c) but for the flare component's continuum luminosity in the TESS-band (6000 – 10000 Å).

and rapid decay. For flare C, although the amplitude of the H α line is comparable to those of flare A and B, we cannot find any clear brightening in TESS light curve. The equivalent width of the H β line also did not exhibit a clear change during this flare. On the other hand, for flare D, we can see a clear white-light flare with an amplitude of 0.6% in TESS band, though the flare amplitude of the H α line is only 50% larger than that of flare C (3 Å). Moreover, the amplitude of flare D in the H β line is 11 Å, which is much larger than that of flare C. Flare D was also detected by multi-color photometry observed with MITSuME, as shown in Fig. 5 (b) and (d). The amplitudes of flare D in the g -, R_C -, and I_C -bands are estimated to be 6.7%, 3.4%, and 0.8%, respectively, by using the MITSuME data around the flare peak in TESS band (from BJD 2458502.227 to 2458502.229). The blackbody fitting to the SED of

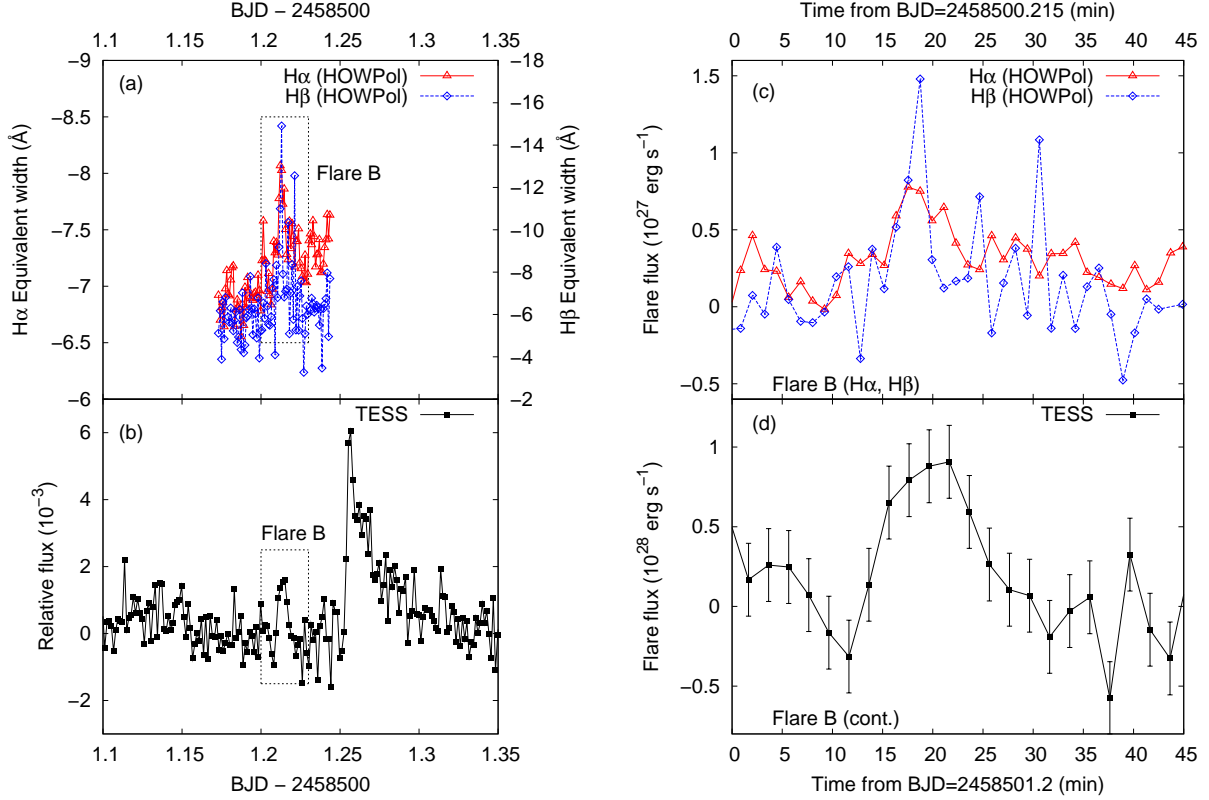


Fig. 4. The axes and symbols are plotted as done in Fig. 3. (a) H α light curve of YZ CMi on January 17. (b) TESS light curve of YZ CMi during the OISTER observations on January 17. (c) H α , H β light curve of flare B. (d) Same as panel (c) but for the flare component's continuum luminosity in the TESS-band.

the flare component around the peak derived from the g -, R_C -, and TESS band data yields an effective temperature of 5900 ± 1000 K, which is comparable to the effective temperature of solar white-light flares (e.g., Watanabe et al. 2013, Kerr & Fletcher 2014, Kleint et al. 2016) and 3000 - 4000 K lower than the typical effective temperature of white-light flares on M dwarfs (e.g., Hawley & Pettersen 1991; Hawley & Fisher 1992; Hawley et al. 2003; Kowalski et al. 2013). According to Kowalski et al. (2019), the effective temperature of flare component estimated from the optical continuum with a wavelength $\lambda > 4000$ Å tends to be low (~ 6000 K) for flares exhibiting large Balmer jump ratio. Kowalski et al. (2013) reported that flares with smaller peak amplitude and longer flare FWHM (full width at half maximum) time tend to show a larger Balmer jump ratio than impulsive flares. As shown in Fig. 6, flare D is not a impulsive flare because of the small peak amplitude (7.6 % in g' -band) and long flare FWHM time (~ 10 min). This morphological property of light curve for flare D is similar to that for flares showing a low-temperature continuum at $\lambda > 4000$ Å.

For the flare C, the peak flux of flare component in the H α line is 1.4×10^{27} erg s $^{-1}$ (Fig. 5 (c)), which is comparable to that of flare D (2.1×10^{27} erg s $^{-1}$; Fig. 6 (c)). However,

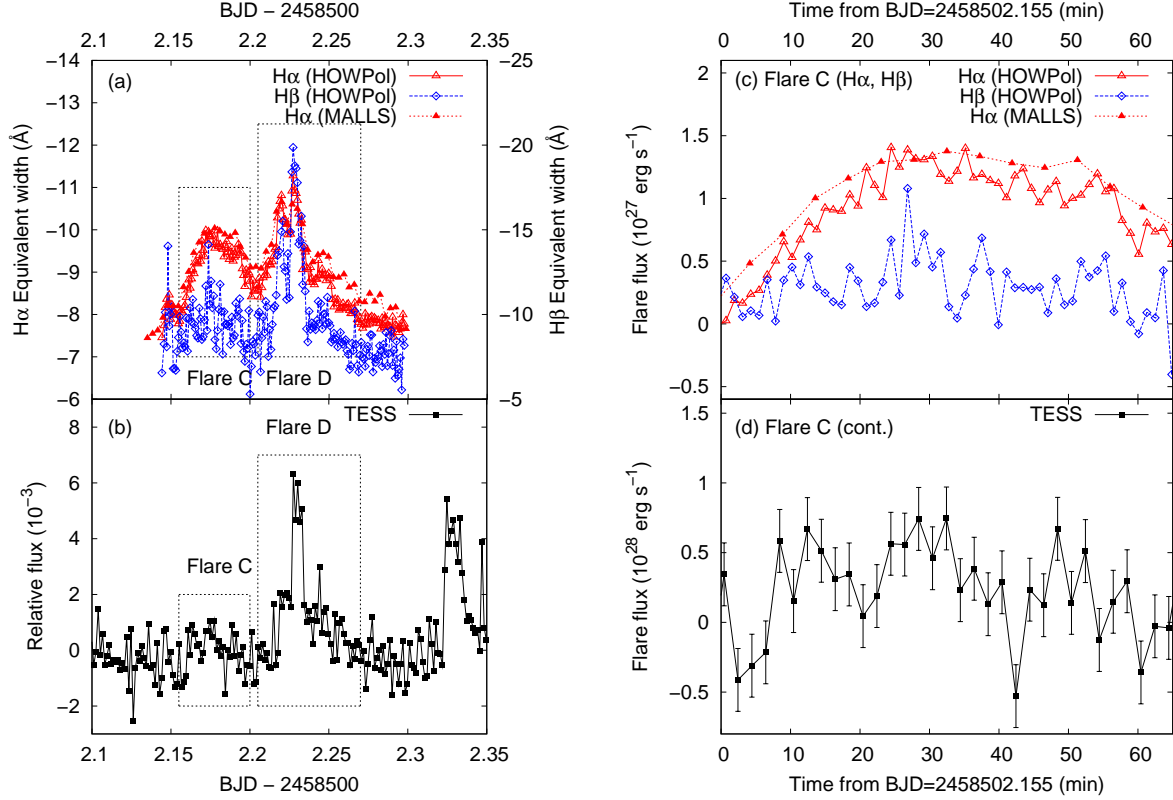


Fig. 5. The axes and symbols are plotted as done in Fig. 3. (a) H α and H β light curves of YZ CMi on January 18. (b) TESS light curve of YZ CMi during the OISTER observations on January 18. (c) H α and H β light curves of flare C. (d) Same as panel (c) but for the flare component's continuum luminosity in the TESS band.

the luminosity of flare component in the TESS-band continuum at the peak timing of flare C is $< 6 \times 10^{27}$ erg s $^{-1}$ (Fig. 5 (d)). This value is $< 1/5$ of the flare D's peak luminosity in the TESS-band (Fig. 6 (d)).

The flare energies released in the optical continuum (TESS band), H α , and H β emission lines for each flare detected by OISTER observations are summarised in Table 2. Among these flares, only flare C did not show a white-light flare. For other flares associated with white-light flares, the flare energy released in the TESS-band continuum ranges from 3×10^{30} erg to 3.6×10^{31} erg. The ratio of the flare energy released in the TESS-band continuum to that released in H α and H β lines ranges from ~ 5 to ~ 20 .

4 Discussion

4.1 White-light and non-white-light flares

In this subsection, we focus on two H α flares (C and D) observed on January 18, 2019. As shown in Fig. 5, the flare C showed a clear increase in the H α emission line, but no significant

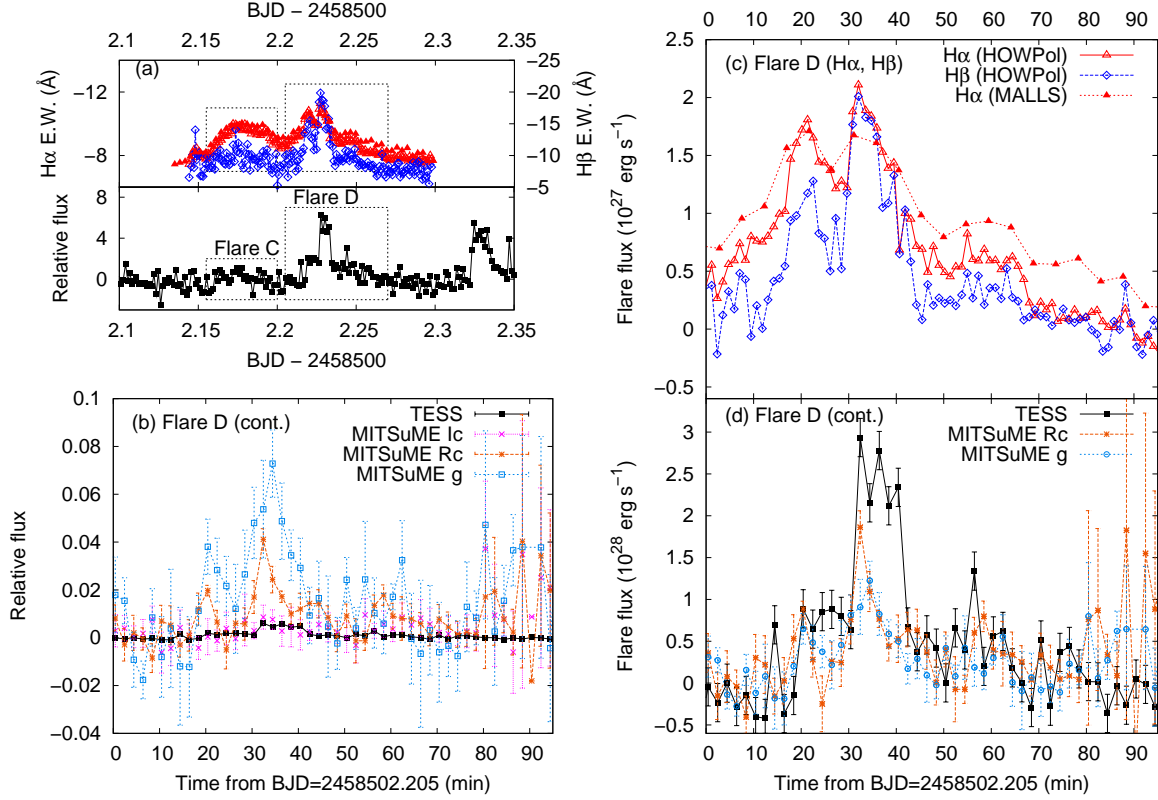


Fig. 6. (a) H α , H β and TESS light curves of YZ CMi on January 18. (b) Light curve of a white-light flare (flare D) on January 18. Filled squares, crosses, asterisks, and open squares represent the brightness change in the TESS- (6000–10000 Å, centered on traditional I_C -band; Ricker et al. 2015) I_C - ($\lambda_0 = 7980$ Å, FWHM= 1540 Å; Bessell 2005), R_C - ($\lambda_0 = 6407$ Å, FWHM= 1580 Å; Bessell 2005), and g -band ($\lambda_0 = 4770$ Å, FWHM= 1380 Å; Fukugita et al. 1996) relative to the pre-flare brightness in each band. Each I_C -, R_C -, and g -band data point and error bar indicate the average value and standard error derived from all data points obtained with MITSuME during each TESS exposure. The effective wavelength (λ_0) and bandwidth ($\Delta\lambda$) are for g -band (Fukugita et al. 1996), $\lambda_0 = 6407$ Å and $\Delta\lambda = 1580$ Å for R_C -band (Bessell 2005), $\lambda_0 = 7980$ Å and $\Delta\lambda = 1540$ Å for I_C -band (Bessell 2005), respectively. (c) H α and H β light curve of flare D. (d) Same as panel (a) but for the flare component's continuum luminosity in the TESS, R_C -, and g -band.

Table 2. List of flares detected by OISTER observations

Flare ID	peak (BJD) ^{*1}	Peak luminosity (10^{27} erg s $^{-1}$)				Energy (10^{31} erg)				Duration (min)
		L_{TESS} ^{*2}	L_{bol} ^{*3}	$L_{\text{H}\alpha}$ ^{*4}	$L_{\text{H}\beta}$ ^{*4}	E_{TESS} ^{*2}	E_{bol} ^{*3}	$E_{\text{H}\alpha}$ ^{*4}	$E_{\text{H}\beta}$ ^{*4}	
A	2458500.260	14	73	1.2	0.8	2.9	15	0.25	0.3	50
B	2458501.212	9	48	0.8	~1.2	0.3	1.8	0.06	0.05	15
C	2458502.177	< 6	< 32	1.4	< 0.5	< 0.4	< 2.1	0.47	< 0.2	> 70 ^{*5}
D	2458502.228	29	155	2.1	2.1	3.6	18	0.18	0.24	35

^{*1} The flare duration and peak time were measured from the H α light curve obtained with Kanata/HOWPol. ^{*2} Luminosity and energy emitted in the TESS bandpass (6000 – 10000 Å). ^{*3} We assumed that the effective temperature of the flare component, temperature and radius of YZ CMi are 10^4 K, 3300 K, and $0.3R_{\odot}$. ^{*4} The flux calibration for the H α and H β lines were performed by using the quiescent spectra taken from Kowalski et al. (2013), g - and R_C -band magnitudes. ^{*5} The flare D started before the flare C ended.

flare was observed in the continuum (Fig. 5). In contrast, flare D showed clear brightening not only in Balmer lines ($H\alpha$ and $H\beta$) but also in the continuum (g , Rc , Ic , and TESS bands). $H\alpha$ and $H\beta$ light curves for flare D show two peaks corresponding to two peaks of white-light flare as shown in Fig. 6. The $H\alpha$ emission line flux at the peak time of flare C is 1.4×10^{27} erg s $^{-1}$, which is comparable to that at the peak of flare D (2.1×10^{27} erg s $^{-1}$). Although the $H\alpha$ line fluxes at flare peaks of C and D are roughly the same, the continuum flux in TESS band at the peak time of flare D (2.9×10^{28} erg s $^{-1}$) is one order of magnitude greater than that of flare C ($< 6 \times 10^{27}$ erg s $^{-1}$).

The differences between flare C and D are the time scale of flare and the ratio of the $H\alpha$ line flux to the continuum flux at the flare peak. The rise time of flare C is much longer than that of that of flare D. In the case flare C, the equivalent width of $H\alpha$ emission gradually increased over ~ 25 minutes and decayed over > 40 minutes. The ratio of the $H\alpha$ line flux to the continuum flux in TESS band was > 0.2 for the flare C. In contrast, the rise time of flare D is ~ 5 minutes, which is comparable to that of flare D observed in continuum light. The peak timings of flare D in $H\alpha$, $H\beta$, and continuum are the same within the time-resolution of observations. The ratio of the $H\alpha$ line flux to the continuum flux in TESS band was ~ 0.07 for the flare D. According to Kowalski et al. 2013, the ratio of the $H\alpha$ emission flux to the total flux at the flare peak ranges from 0.0005 to 0.10 for various types of flares on M dwarfs. The ratio of the $H\alpha$ line flux to the total flux at the peak time of the gradual flares showing slow rise/decay ($L_{H\alpha}/L_{bol.} \sim 3\text{-}10\%$) tends to be larger than that of impulsive flares ($< 1.7\%$). The difference in the flux ratio of $H\alpha$ and continuum between the flare C and flare D agree with this tendency.

According to 1-dimensional radiative hydrodynamic model calculation of stellar flares on M dwarfs by Namekata et al. (2020b) using the RADYN code (Carlsson & Stein 1997; Allred et al. 2015), the $H\alpha$ line and continuum intensity increase as the energy deposition rate increases and the correlation between the intensity of $H\alpha$ line ($I_{H\alpha}$) and that of continuum ($I_{cont.}$) can be expressed by $I_{cont.} \propto I_{H\alpha}^{0.5}$. This suggests that the fraction of continuum intensity relative to the $H\alpha$ intensity increases as the continuum intensity increases. In the case of the flare caused by the larger non-thermal electron flux, the ratio of the continuum intensity to the $H\alpha$ intensity is much larger than that for the flare caused by the smaller non-thermal electron flux. This non-linear correlation between the intensity of $H\alpha$ line and that of continuum suggests that the observed difference in the ratio of the continuum flux to the $H\alpha$ flux between the flare C and flare D can be explained by the difference in the energy deposition rates. This interpretation is also consistent with the fact that the rise time of flare C (small deposition rate) is longer

than that of flare D (large deposition rate). The long rise time of flare C suggest that flare C is actually a group of many small flares for which detectable white light emission is not expected. In addition to the continuum flux, the $H\beta$ line flux at the peak time of flare C is also smaller than that at the peak time of flare D. The ratio of $H\beta$ line flux to the $H\alpha$ line flux ($H\beta/H\alpha$) is < 0.4 for flare C and ~ 1.0 for flare D. $H\beta/H\alpha$ depends on the electron density, temperature and optical depth according to Drake & Ulrich (1980). Since the optical depth of the $H\beta$ line is smaller than that of the $H\alpha$, the $H\beta$ line flux may behave like the continuum rather than the $H\alpha$ line flux during the flare. The smaller value of $H\beta/H\alpha$ for flare C than that for flare D suggests that the electron density of the flare region for flare C is smaller than that for flare D. This may be consistent with the non-thermal electron flux for flare C being smaller than that for flare D.

As mentioned above, although the intensity of $H\alpha$ line from the flare region for flare C is expected to be smaller than that for flare D, the peak $H\alpha$ luminosity of flare C is comparable to that of flare D. This may suggest that the area of flare region for flare C is larger than that for flare D. As we discuss in later section, the larger area of flare region for flare C would lead to the longer flare duration. Solar non-white light flares have longer soft X-ray flare durations than white-light flares with the similar GOES X-ray class (e.g., Watanabe et al. 2017). This tendency is consistent with the differences in the duration and peak continuum flux between the flare C and flare D.

4.2 $H\alpha$ line profile changes during flares C and D

During flare C, the profile of $H\alpha$ line showed blue asymmetry (Fig. 7). As shown in Fig. 8, the velocity of the blue-shifted excess component at the peak time of flare C is $-85 \pm 3 \text{ km s}^{-1}$. The blue-shifted excess component with the line of sight velocity of $-80 - -100 \text{ km s}^{-1}$ has been seen for 60 minutes during flare C (Fig. 9). Around the peak time of flare C, roughly 1/4 - 1/3 of the $H\alpha$ emission of flare component was emitted from the blue-shifted excess component. On the other hand, no clear asymmetry in the $H\alpha$ line profile was observed during the flare D (Fig. 7 and 8).

Since the velocity of blue-shifted component observed during flare C is one order of magnitude larger than the stellar rotation velocity ($v \sin i \sim 6 \text{ km s}^{-1}$; e.g., Houdebine et al. 2016), observed blue asymmetry cannot be explained by the rotationally modulated emission from the co-rotating prominence (e.g., Collier Cameron & Robinson 1989).

According to Fisher et al. (1985), when the non-thermal electron flux is low, a weak

chromospheric evaporation with the upward velocity $< 30 \text{ km s}^{-1}$ occurs (gentle evaporation). The threshold for the gentle evaporation depends on the energy spectra of non-thermal electron beam (low-energy cutoff and power-law index; Fisher 1989). As discussed above, the weak non-thermal electron flux is suggested from the weak continuum intensity relative to the $\text{H}\alpha$ intensity for the flare C. The observed velocity of blue asymmetry during flare C ($80\text{-}100 \text{ km s}^{-1}$) is a few times larger than the theoretical prediction for solar flares and that of blue asymmetry observed during the gradual phase of solar flares (e.g., Schmieder et al. 1987).

The Doppler velocity of observed blue asymmetry is comparable to that of blue asymmetry observed in chromospheric lines during the initial phase of solar flares, which is proposed to be caused by the cool plasma lifted up by the expanding hot plasma (e.g. Tei et al. 2018, Li et al. 2019). However, the duration of these blue asymmetries (a few min) are roughly two orders of magnitude shorter than that of the blue asymmetry observed during flare C (~ 60 min). Honda et al. (2018) reported the similar long-duration $\text{H}\alpha$ flare showing blue asymmetry in the $\text{H}\alpha$ line profile on the M4.5 dwarf EV Lac. The Doppler velocity of blue-shifted excess component for this event is $\sim 100 \text{ km s}^{-1}$ and the blue asymmetry has lasted for > 2 hours. Since there were no high-precision photometric data for the $\text{H}\alpha$ flare showing a blue asymmetry reported by Honda et al. (2018), it is unclear whether the typical long duration $\text{H}\alpha$ flares with blue asymmetry are non-white-light flares as flare C or not.

The observed velocity of the blue asymmetry during flare C is also comparable to the velocity of $\text{H}\alpha$ surges (e.g. Canfield et al. 1996) and that of prominence/filament eruptions (e.g., Gopalswamy et al. 2003) of the Sun. In case of stellar flares, since we cannot obtain spatial information of stellar surface, such eruptions and surges may also be possible causes of the blue asymmetry in the $\text{H}\alpha$ line associated with flares. Vida et al. (2016) reported several flares on the M4 dwarf V374 Peg exhibiting blue asymmetry whose Doppler velocity ranges 200 to 400 km s^{-1} . The duration of these blue asymmetries ranges from 10 to 30 minutes. The similar high-velocity blue asymmetry has been observed during a flare on AT Mic (Gunn et al. 1994). Such high-velocity blue asymmetries during stellar flares are considered to cause stellar CMEs (e.g., Vida et al. 2016). According to Gopalswamy et al. (2003), the average velocity of the core of CMEs ($\sim 350 \text{ km s}^{-1}$) and average CME velocity ($\sim 610 \text{ km s}^{-1}$) are ~ 4 and ~ 8 times larger than that of the associated prominences ($\sim 80 \text{ km s}^{-1}$), respectively. This indicates that the most prominences accelerate as they erupt. If the similar acceleration mechanisms would work on YZ CMi, although the velocity of prominence eruption ($\sim 100 \text{ km s}^{-1}$) is smaller than the escape velocity at the stellar surface ($\sim 600 \text{ km s}^{-1}$ for YZ CMi), the upward-moving material would be accelerated to $\sim 400\text{-}800 \text{ km s}^{-1}$. Since this value is larger than the escape velocity

at $\sim 2\text{-}3 R_{\text{star}}$ ($\sim 350\text{-}420 \text{ km s}^{-1}$), even the prominence eruption with the velocity of $\sim 100 \text{ km s}^{-1}$ could cause a CME. However, it is still unclear whether the prominence eruptions on M dwarfs can cause the stellar CMEs. Crosley & Osten (2018) performed optical and low-frequency radio observations of the M4 dwarf EQ Peg and found no signature of type II bursts, which are believed to be excited by shocks driven by CMEs, during the observed flares. One interpretation for the absence of type II bursts is the magnetic suppression of CMEs in active stars. Numerical studies by Drake et al. (2016) and Alvarado-Gómez et al. (2018) suggest that if the flare region has strong overlying magnetic fields, CMEs will be suppressed. According to Morin et al. (2008), rapidly-rotating mid-M ($\sim M4$) dwarfs such as YZ CMi have mainly axisymmetric large-scale poloidal fields. In the case of YZ CMi, the magnetic energy in dipole mode accounts for ~ 70 percent of the whole magnetic energy, and such large-scale and strong dipole magnetic fields may cause the suppression of CMEs. Another interpretation for the absence of stellar type II radio burst is that CMEs propagating in the corona/wind of active M dwarfs are radio-quiet for ground-based instruments. Mullan & Paudel (2019) proposed that due to the large Alfvén speed in the corona of active M dwarfs, CMEs from these stars could not satisfy the conditions for the generation of type II radio bursts. According to 3D magnetohydrodynamic simulations by Alvarado-Gómez et al. (2020), while CMEs from active M dwarfs can generate shocks in the corona, type II radio burst frequencies are down to the ionospheric cutoff and therefore it is difficult to detect type II radio bursts from active M dwarfs by ground-based instruments.

As shown in Fig. 9, the velocity of the blue-shifted excess component is almost constant ($80 - 100 \text{ km s}^{-1}$) during the flare C and the $\text{H}\alpha$ line flux from the blue-shifted component decreases as the later part of the flare C. In the case of solar CMEs, a prominence forms the core of a CME (e.g., Gopalswamy 2015) and the prominence material can be observed in the $\text{H}\alpha$ line only at early stages. If the prominence on YZ CMi forms the core of a CME and $\text{H}\alpha$ emission from the prominence would disappear as the height of the prominence increases, then the observed blue-shifted excess would come from the prominence at the lower layer and the velocity of the blue asymmetry would not change so much during the flare C. The intensity of the blue-shifted excess may decrease as the mass of the cool material at lower layer decreases. Another interpretation for the persistent blue-asymmetry with a constant velocity for ~ 1 hour associated with flare C is that it is caused by the ongoing magnetic reconnection and plasma evaporation in the multi-threaded coronal loops (e.g. Warren 2006). If upward velocities of evaporated plasma in each coronal loop would be roughly the same, the velocity of blue-shifted excess would also be constant during the flare. However, since our observations are limited (only

optical H α line is used here), it is difficult to distinguish whether the observed blue asymmetry was caused by a prominence eruption, which would cause a stellar CME, or by the chromospheric evaporation in coronal loops. Time-resolved and high-resolution X-ray spectroscopy of stellar flares (e.g., Argiroffi et al. 2019), EUV observations for the coronal dimming associated with stellar flares (e.g., Jin et al. 2020), and radio observations for stellar type II bursts (e.g., Crosley & Osten 2018) simultaneously with optical spectroscopy are necessary to investigate the connection between the blue asymmetries in the chromospheric lines and stellar CMEs.

As shown in Fig. 9, the equivalent width of the H α emission from the blue-shifted excess is $\sim 1 \text{ \AA}$, which corresponds to the luminosity of H α emission of $L_{\text{H}\alpha} \sim 6 \times 10^{26} \text{ erg s}^{-1}$. According to the Non-LTE model of the solar prominence by Heinzel et al. (1994a), the flux of the H α line ($F_{\text{H}\alpha}$) is roughly $10^{5.5} \text{ erg s}^{-1} \text{ cm}^{-2} \text{ sr}^{-1}$, if we assume that the optical thickness of the H α line ($\tau_{\text{H}\alpha}$) ranges from 1 to 10. If we assume the physical parameters of the prominence on YZ CMi are similar to that on the Sun, the observed luminosity of H α emission suggests that the emitting area of blue-shifted H α emission (A) would be $\sim 3 \times 10^{20} \text{ cm}^2$, which is roughly 10% of the area of visible stellar surface. This value is comparable to the area of starspots estimated from the amplitude of rotational variations. By adopting the electron density (n_e) - H α line flux ($F_{\text{H}\alpha}$) correlation and the correlation between the electron density (n_e) and total Hydrogen density (n_H) from Heinzel et al. (1994a), $n_e \sim 10^{10.5} - 10^{11} \text{ cm}^{-3}$ for $F_{\text{H}\alpha} \sim 10^{5.5} \text{ erg s}^{-1} \text{ cm}^{-2} \text{ sr}^{-1}$ and $n_H \sim 10^{11} \text{ cm}^{-3}$. Although the H α emission is likely from a region whose width along the line of sight is consistent with an optical depth of unity (which would be much smaller than the prominence size), in order to estimate the upper limit of prominence mass, we assumed that the geometrical thickness of the upward-moving prominence is comparable to the size of the prominence ($A^{0.5}$). Under this assumption, the total mass of the upward-moving material (M) can be written as the following form:

$$M \sim A^{1.5} n_H m_H \sim (3 \times 10^{20})^{1.5} 10^{11} 1.7 \times 10^{-24} \sim 10^{18} \text{ (g)}, \quad (3)$$

where m_H is the mass of Hydrogen atom. In the case of solar prominence, the Hydrogen column density (N_H) is estimated to be approximately $1 - 5 \times 10^{19} \text{ cm}^{-2}$ (e.g., Gilbert et al. 2005 for eruptive prominence; Landi & Reale 2013 for prominence blobs; Heinzel et al. 2008 for quiescent prominence). According to Dunstone et al. (2006), the column density of the co-rotating prominence on the K3 dwarf BO Mic (= HD 197890) is estimated to be $N_H \sim 3 \times 10^{19} \text{ cm}^{-2}$. If we assume the column density of the upward-moving prominence is roughly the same order of magnitude with those of the solar and stellar prominences, the mass of the prominence can be estimated to be

$$M \sim AN_H m_H \sim 3 \times 10^{20} (1-5) \times 10^{19} 1.7 \times 10^{-24} \sim (0.5-2.5) \times 10^{16} \text{ (g)}. \quad (4)$$

The estimated mass of the upward-moving material is the same order of magnitude with those estimated by Vida et al. (2016) (V374 Peg) and Moschou et al. (2019) (DENIS 1048-39 and AD Leo). Since the observed upward velocity is $80 - 100 \text{ km s}^{-1}$, the kinetic energy of the upward-moving material is estimated to be the order of $10^{29.5} - 10^{31.5} \text{ erg}$, which is roughly the same order of magnitude with the energy emitted in TESS-band continuum ($< 4 \times 10^{30} \text{ erg}$) or in the $H\alpha$ line ($5 \times 10^{30} \text{ erg}$). According to Moschou et al. (2019), the luminosity in GOES X-ray band ($1-8 \text{ \AA}$; $L_{X,GOES}$) can be estimated from the $H\alpha$ luminosity ($L_{H\alpha}$) by using the following linear relation:

$$L_{X,GOES} = 16L_{H\alpha}. \quad (5)$$

Then the X-ray flare energy of the flare C in the GOES $1-8 \text{ \AA}$ band is estimated to be $8 \times 10^{31} \text{ erg}$ if we assume the X-ray light curve shape is similar to that of $H\alpha$. In the case of X-class solar flares, the X-ray energy in the GOES $1-8 \text{ \AA}$ band is roughly 1/20 of the total energy radiated from the soft X-ray (SXR) emitting plasma (Emslie et al. 2012). According to Emslie et al. (2012) and Aschwanden et al. (2017), the kinetic energy of solar CMEs is 1 – 10 times greater than the total energy radiated from the SXR-emitting plasma. In the case of flare C, the kinetic energy ($10^{29.5} - 10^{31} \text{ erg}$) estimated from the blue-asymmetry in $H\alpha$ line is at least ~ 2 order of magnitude smaller than the thermal energy ($\sim 10^{33} \text{ erg}$) estimated from the energy emitted in $H\alpha$ line. As listed in Table 2, the upper limit of flare energy emitted in the TESS-band continuum for flare C is comparable to or smaller than that emitted in the $H\alpha$ line and two orders of magnitude smaller than the total SXR energy. These suggest that the upper limit of bolometric energy for flare C listed in Table 2 may be very small compared to the true bolometric energy. However, since the SXR flare energy estimated from the empirical relation between the X-ray luminosity and $H\alpha$ luminosity (equation 5) may have a large uncertainty, it is unclear whether the true bolometric energy for flare C is much larger than the flare energy estimated from the TESS light curve. Fig. 10 represents the mass and kinetic energy of prominence eruptions and CMEs as a function of X-ray flare energy in the GOES $1-8 \text{ \AA}$ band. The estimated mass of the upward-moving material for the flare C is roughly on the relation between the mass and flare energy for stellar flares. The masses for stellar events lie along or slightly below the extrapolated solar trend. The estimated kinetic energy for the flare C appears to be good agreement with the relation between the kinetic energy and X-ray flare energy for stellar flares. However, the kinetic energies for stellar events, including the flare C, are roughly two orders of magnitude smaller than the extrapolated solar trend as pointed out by Moschou

et al. (2019). Since the kinetic energies for stellar events are derived from the blue-shifted enhancement in chromospheric lines (e.g., Balmer lines) or X-ray dimming associated with the enhancement of the hydrogen column density, these stellar events may not be CMEs but prominence/filament eruptions. As mentioned above, the average velocity of CMEs on our Sun is ~ 4 -8 times faster than that of prominence/filament eruptions (e.g., Gopalswamy et al. 2003). Therefore the kinetic energy for stellar events estimated from the velocity of upward-moving prominence would be 1-2 orders of magnitude smaller than the solar CME trend.

4.3 Rotational modulations

As shown in Fig. 1, YZ CMi shows the sinusoidal brightness variations with the period of 2.7737 ± 0.0014 d and full-amplitude of 3.6 %. The maximum timing of observed flux can be represented by the following equation:

$$T_{\text{max;BJD}} = 2458498.329 + 2.7737 \times E, \quad (6)$$

where E is the number of rotation. These variations are thought to be caused by the rotation of the star with spotted surface (e.g., Berdyugina 2005, Strassmeier 2009) and the amplitude of rotational modulations is thought to correlate with the size of starspots. Fig. 11 shows the rotational modulation of YZ CMi in continuum light (g -, R_C -, and TESS bands) plotted with that of the equivalent width of $H\alpha$ line. The rotational modulations in g -, R_C -, and TESS bands can be represented by sinusoidal functions in phase.

The amplitude of rotational modulations in continuum light increases as the wavelength decreases. The sinusoidal fits to the data yield the full-amplitude of 9.8 % in g -band and 7.4 % in R_C -band, respectively. Starspots are thought to be cooler than surrounding photosphere as the sunspots are. The temperature difference between spots and unspotted photosphere determine how the amplitude of rotational modulation depends on the wavelength. In addition to the temperature difference between spots and unspotted regions, the wavelength dependence of limb-darkening coefficient also causes the amplitude of rotational modulation depends on the wavelength. Since the limb-darkening coefficient of low mass stars increases as the wavelength decreases in optical and near infra-red bands (e.g., Claret 2000), the effective size of the apparent stellar disk decreases as the wavelength decreases. Therefore the amplitude of rotational modulations increases as the wavelength decreases. We estimated the change in the spot coverage due to the stellar rotation from the amplitude of rotational modulations in g -, R_C -, and TESS bands. As mentioned above, not only the temperature difference between spots and unspotted photosphere, but also the limb-darkening coefficient affect the amplitude of ro-

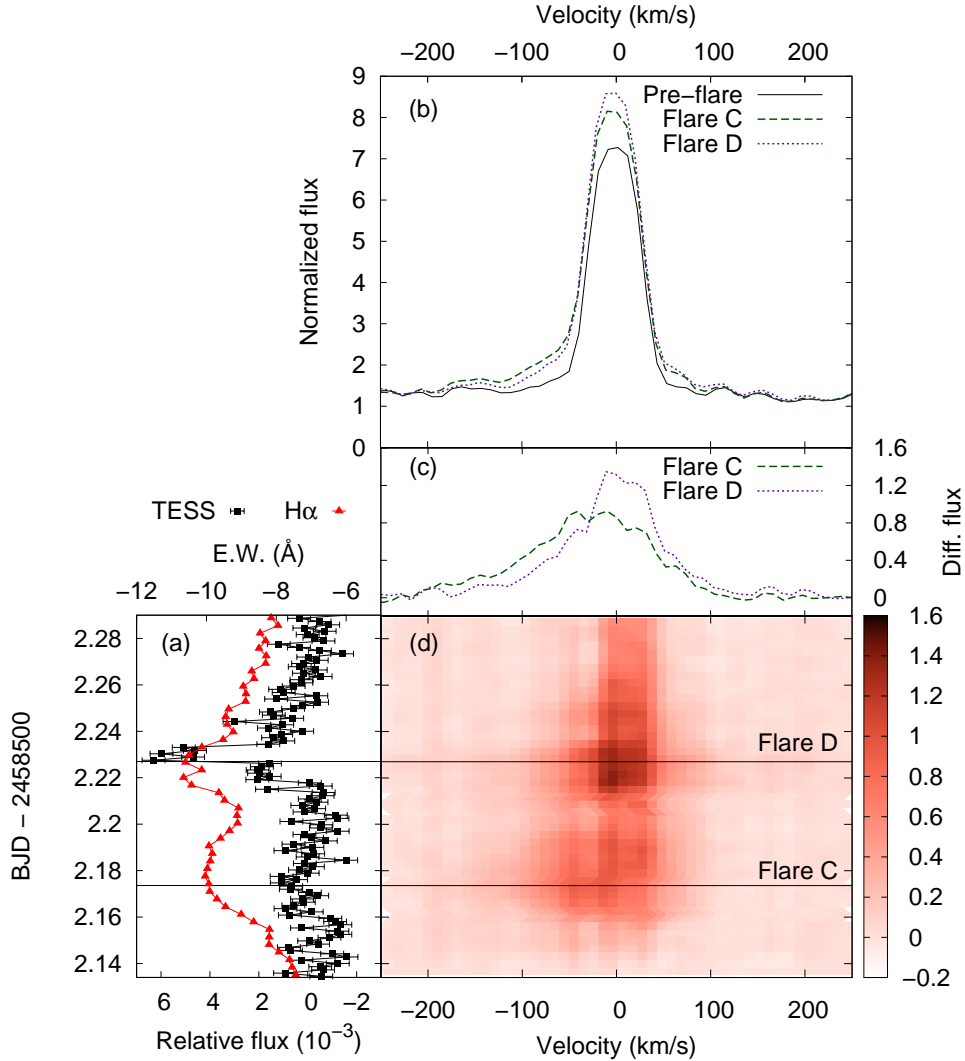


Fig. 7. (a) Light curve of YZ CMi during flare C and D. Filled squares (black) and triangles (red) represent continuum flux relative to the average flux observed with TESS and equivalent width of H α line observed with Nayuta/MALLS. The vertical axis indicates the time of observation in Barycentric Julian Date (BJD). The lower and upper horizontal axes represent continuum flux relative to the average stellar flux and equivalent width in unit of \AA , respectively. (b) Line profile of H α emission line. The horizontal and vertical axes represent the Doppler velocity from H α line center and flux normalized by the continuum. Solid (black), dashed (green), and dotted (purple) lines indicate the line profile before flares (BJD 2458502.135), that at the peak timing of flare C (BJD 2458502.177) and that of flare D (BJD 2458502.227). (c) Same as (b), but for the line profile changes from the pre-flare to the peak times of flare C and D. (d) Time evolution of H α line profile. The horizontal and vertical axes represent the Doppler velocity from H α line center and time of observation. The color map represents the line profile changes from the pre-flare profile.

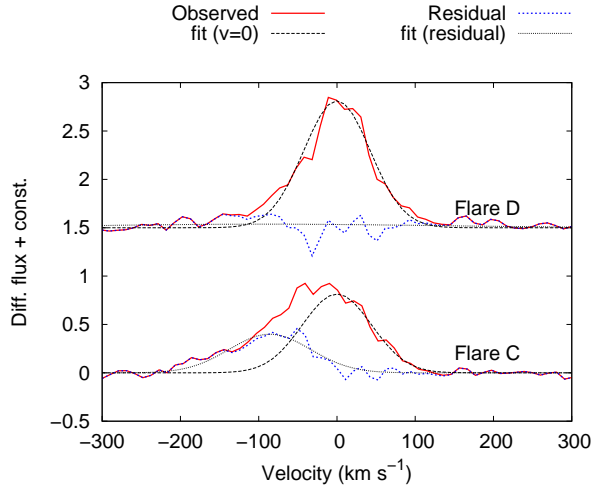


Fig. 8. $H\alpha$ line profile changes from the pre-flare (BJD 2458502.135) to the peak times of flare C (BJD 2458502.177; lower) and D (BJD 2458502.227; upper). Red solid lines indicate the observed line profile changes. Black dashed lines represent a Gaussian fit assuming the line-of-sight velocity of 0 km s^{-1} to the red-part ($> 0 \text{ km s}^{-1}$) of the observed line profile changes. Blue dotted lines indicate residuals between the observed line profile changes and the Gaussian fits (thin-dashed lines). Black dash-dotted lines represent a Gaussian fit to the residuals (blue dotted lines). The line-of-sight velocity of the residual component (blue enhancement) at the peak time of the flare C is $-85 \pm 3 \text{ km s}^{-1}$.

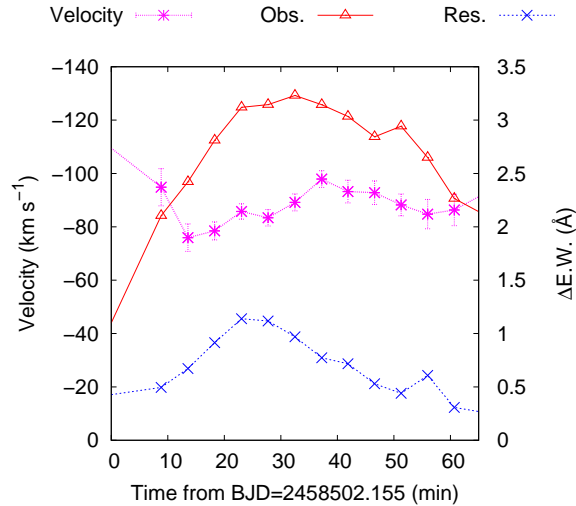


Fig. 9. Time variation of the line-of-sight velocity and equivalent width of the blue-shifted enhancement during the flare C. Magenta asterisks and blue crosses indicate the velocity and equivalent width of blue-shifted excess component. Red open-triangles indicate the equivalent width of flare component (change in the equivalent width from the pre-flare state).

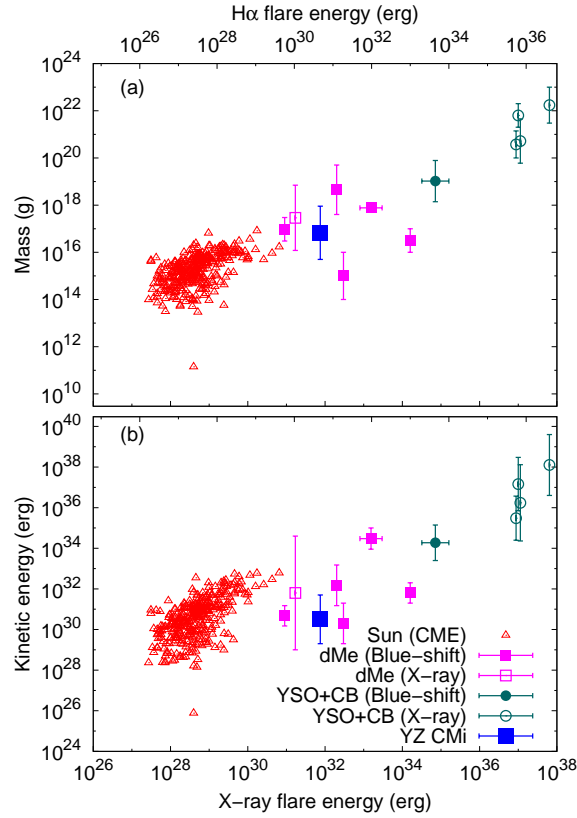


Fig. 10. (a) Mass of CMEs/prominences as a function of flare energy. Upper and lower horizontal axis represent the flare energies emitted in the H α emission line and in X-ray (GOES 1–8 Å band), respectively. The H α flare energy is converted to the GOES X-ray flare energy by using equation (5). Open triangles (red) represent the CME mass of solar events taken from Yashiro & Gopalswamy (2009). X-ray energy of associated solar flares are derived from the X-ray fluence in GOES 1–8 Å band. Filled squares (magenta) and filled circles (cyan green) indicate the CME/prominence mass of stellar events on M-dwarfs (dMe), young stellar objects (YSO) and close binary systems (CB) estimated from the blue-shifted enhancement of chromospheric lines. Open squares and filled circles also indicate the mass of stellar events on M-dwarfs, young stellar objects and close binary systems estimated from the X-ray dimming. Mass and X-ray energy for these events are taken from Moschou et al. (2019). Large filled square (blue) indicates the mass of upward-moving material for the flare C on YZ CMi. The upper and lower error bars for the flare C on YZ CMi represent the mass of upward-moving material estimated in (3) and (4). (b) Same as (a) but for the Kinetic energy of CMEs/prominences as a function of flare energy.

tational modulations. We estimated the temperature difference between spots and unspotted photosphere ($\Delta T = T_{\text{star}} - T_{\text{spot}}$) by using the following equation,

$$\Delta T(T_{\text{star}}) = T_{\text{star}} - T_{\text{spot}} = 3.58 \times 10^{-5} T_{\text{star}}^2 + 0.249 T_{\text{star}} - 808, \quad (7)$$

which was derived from the second order polynomial fit to the data for all stars except for EK Dra in table 5 of Berdyugina (2005). In the case of YZ CMi ($T_{\text{star}} = 3300$ K; e.g., Gaidos & Mann 2014), the the temperature difference between spots and photosphere is estimated to be $\Delta T \sim 400$ K. According to Baroch et al. (2020), the temperature difference between the photosphere and spot estimated is estimated to be ~ 200 K (178.6-273.4; best model: 199.7 ± 9.6 K) from chromatic radial velocities. We assumed that the limb-darkening law is represented by

$$I(\mu)/I(1) = 1 - \sum_{k=1}^4 a_k (1 - \mu^{k/2}), \quad (8)$$

where $I(\mu)/I(1)$ is the intensity of the stellar disk relative to the intensity at the disk center and a_k are the limb-darkening coefficients (Claret 2000). The parameter μ is given by $\mu = \cos\theta$, where θ is the angular distance from the center of the disk. a_k are taken from tables in Claret et al. (2012) for the star with the effective temperature of 3300 K and surface gravity ($\log g$) of 5.0. For YZ CMi, the effective area of stellar disk would be reduced by $\sim 22\%$ in g -band, $\sim 20\%$ in R_C -band and $\sim 14\%$ in TESS-band compared with the geometric (apparent) area. The amplitude of the rotational brightness modulation in g , R_C , and TESS bands (9.8 %, 7.4 %, and 3.6 %) correspond to the rotational change in spot coverage of 11 %, 9.7 %, and 6.2 % if we assume $\Delta T = 400$ K. For $\Delta T = 200$ K, the rotational change in spot coverage is estimated to be 11 % (from TESS band) and 17 % (from g - and R_C - band). This result suggests that at least $\sim 10 - 20$ % of stellar surface would be covered by starspots. The estimated spot coverage is comparable to those estimated by Zboril (2003) and Baroch et al. (2020). Since the amplitude of rotational modulations depends on the inclination angle and spot latitude, it should be noted that these values are lower limits. The inclination angle of YZ CMi is estimated to be 60° (Morin et al. 2008) and $36_{-14}^{+17}^\circ$ (Baroch et al. 2020). The Zeeman-Doppler Imaging observation by Morin et al. (2008) found a strong spot near the visible pole. These results suggest that the total spot coverage would be larger than the value estimated from the amplitude of rotational modulations.

During the OISTER observations, the intensity of the $H\alpha$ line shows the anti-correlated rotational modulation with that in continuum light (Fig. 11 (a)). Since the amplitude of rotational modulation in $H\alpha$ (11 %) is slightly larger than that of the rotational modulation in R_C -band (7.4 %), the rotational modulation in $H\alpha$ line cannot be produced only by that in

R_C -band if we assume that the $H\alpha$ line flux is constant over the rotation phase and only the continuum intensity changes due to the rotation. On the other hand, the rotational modulation in $H\alpha$ line cannot be seen in the data obtained during the APO observations. The $H\alpha$ line intensity is almost constant over the rotation phase (Fig. 11 (b)). These results suggest that bright regions in $H\alpha$ line are concentrated at the darker side in continuum (rotation phase of 0.5) during the OISTER observation period, and the $H\alpha$ line intensity at the brighter side in the continuum (rotation phase of 0) has increased before or during the APO observations. As shown in Fig. 1 (b) and (c), the number of flares during the OISTER observations is smaller than that during the APO observations, and large flares occurred just before and during the APO observations at the rotation phase of $\sim 0.7 - 0.8$. This suggests that the $H\alpha$ intensity of the existing active region, which can be seen around the rotation phase of $\sim 0.7 - 0.8$, has increased due to the new flux emergence that makes the active region more flare-productive, or new flare-productive active region has appeared at the longitude corresponds to the rotation phase of $\sim 0.7 - 0.8$. Since such active region(s) would be bright in $H\alpha$ and can change the rotational modulations in the $H\alpha$ line. Since the rotational modulations in the continuum are almost the same between these two observations while the rotational modulations in $H\alpha$ line are different, the sizes and locations of starspots may not change, or the size of starspots associated with the new active region may not be so large. According to VIDA et al. (2016), anti-correlated modulations in the $H\alpha$ line and in the optical continuum were reported in an active M dwarf V374 Peg during the observations in 2009. However, this anti-correlation is unclear for the data obtained in 2005 and 2006. These difference in rotational modulations between the data in 2005-2006 and in 2009 may also be explained by the difference in the surface distribution of active regions.

Fig. 12 shows (a) rotational brightness variation, (b) flare frequency as a function of rotation phase, and (c) bolometric energy of each flare as a function of rotation phase. There is no clear correlation between the rotation phase and flare activities such as flare frequency and the energy of the largest flare in each phase bin. Similar results have been reported by Hawley et al. (2014) and Silverberg et al. (2016) in an active M dwarf GJ 1243, and by Doyle et al. (2020) in active solar-type stars. They found that the flare frequency and flare energy do not depend on rotation phase. Hawley et al. (2014) and Davenport et al. (2015) proposed two possible interpretations for this property: (1) The large fraction of polar region is covered by starspots and flares come from the large starspots near the pole. The rotational modulation of stellar brightness in the optical continuum is mainly caused by the rotational change in the apparent area of starspots near the pole if the location of polar spot is slightly shifted from the

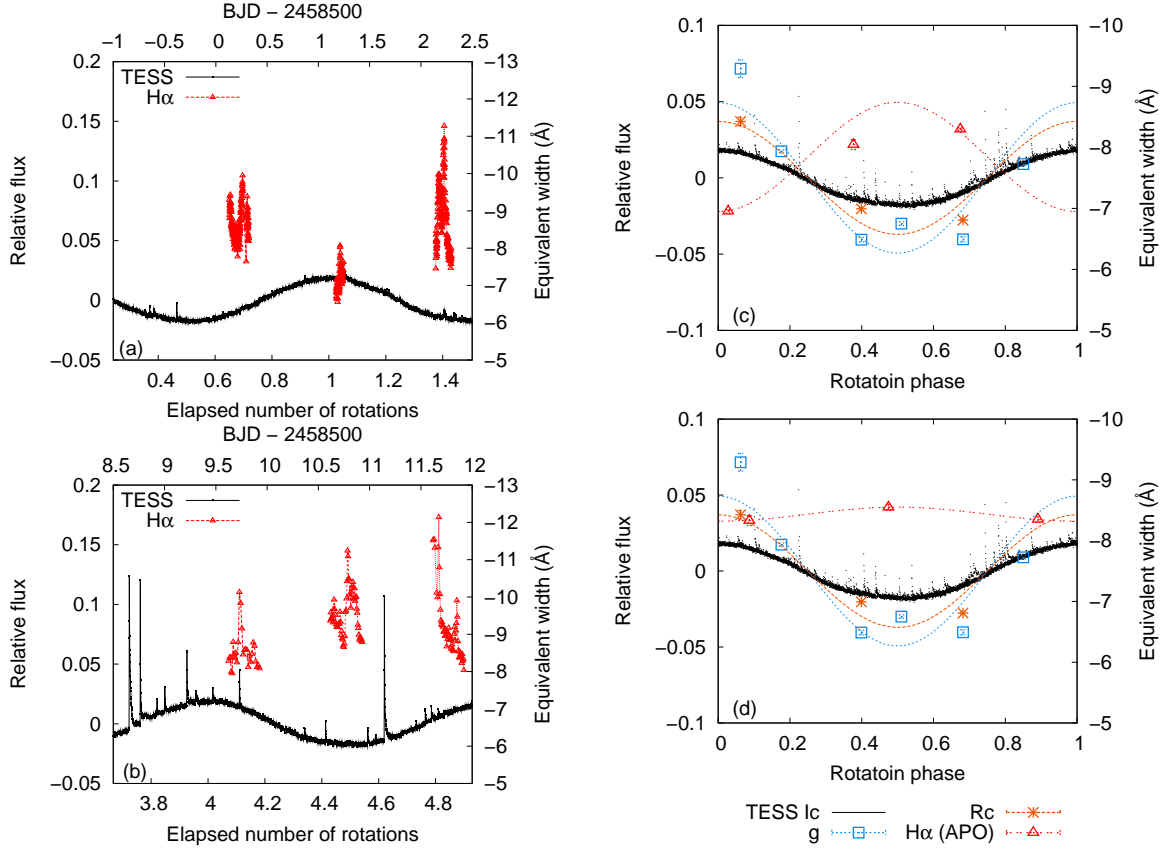


Fig. 11. (a) TESS light curve (black line) and $H\alpha$ equivalent width (red open triangles) of YZ CMi around OISTER observation period. The left and right vertical axis indicate the relative flux in TESS band and equivalent width of $H\alpha$ emission line. The horizontal axis indicates the number of stellar rotation since BJD 2458498.329. (b) Same as (a) but for the light curve around APO observation period. (c) Rotational brightness modulations in g - (blue open-squares), R_C - (orange asterisks), TESS bands (black dots; large flares were excluded) observed during the TESS cycle 7 and the rotational modulation of the $H\alpha$ equivalent width (red triangles) obtained by OISTER observations. g -band, R_C -band, and $H\alpha$ data indicate the average value during each observation run except for the data during flares. The rotation phase was calculated from equation (6). Blue dotted, orange dashed, and red dash-dotted lines indicate sinusoidal fits to g -band, R_C -band, and $H\alpha$ line data. (d) Same as (c) but for the rotational modulations of the equivalent width of $H\alpha$ emission line obtained by APO observations.

rotation axis or the polar spot is not completely axisymmetric. Since the starspots near the pole always can be seen from the observer, the flare frequency does not depend on the rotation phase. (2) The most of flares come from many relatively small active regions which contain large amount of stellar magnetic flux (Reiners & Basri 2009), while the polar spot is associated with the global dipolar magnetic field (Morin et al. 2008). Since these many small active regions are distributed across longitude (e.g., Namekata et al. 2020a; Takasao et al. 2020), they cannot produce significant brightness modulation (e.g., Schrijver 2020) compared to that from the large polar spot and the flare frequency would not depend on the rotation phase. A strong correlation between the core emission of Ca H and K lines and the magnetic field strength (e.g., Schrijver et al. 1989, Notsu et al. 2015) suggests that the origin of chromospheric emission is

magnetic. As mentioned above, although the rotational modulations in H α line are different between two observations, the rotational modulations in continuum are almost the same. The possible explanations for the observed changes in rotational modulations based on the possible interpretations for the rotational modulations of flare frequency are as follows: During the low-activity period, both rotational modulations in the optical continuum and in the H α line are mainly produced by the polar spot and surrounding active regions. Since both the apparent area of polar spot and that of surrounding active regions change as the star rotates, rotational modulations in the continuum and in the H α line would be anti-correlated. In the case of high-activity period, although the rotational modulation in optical continuum is also produced by the polar spot, most of the H α line emission come from many relatively small active regions which are distributed across longitude. Therefore the H α line intensity does not depend on the rotation phase during the high-activity phase. Since the chromospheric emission is thought to be correlated with the flare activity, these results on the rotational modulation of H α line intensity suggest that the constant flare frequency over the rotation phase on active M dwarfs can be explained if the most of flares would occur on many smaller active regions across the entire stellar longitude.

4.4 Flare duration vs. flare energy

Fig. 13 shows the scatter plot of the duration (e -folding time) of flares on YZ CMi observed with TESS as a function of flare energy. We estimated the e -folding time by the exponential fit to the data for each flare from the flare peak time ($t = t_{\text{peak}}$) to $t = t_{\text{peak}} + 2(t_{1/e} - t_{\text{peak}})$, where $t_{1/e}$ is the time that the flare flux decays to $1/e$ of the peak flux. We can see a positive correlation between the flare duration (τ_{flare}) and the bolometric flare energy (E_{flare}). The duration of flares increases with energy as $\tau_{\text{flare}} \propto E_{\text{flare}}^{0.21 \pm 0.04}$. The power-law slope of the correlation between the flare duration and energy for flares on YZ CMi is smaller than that for flares on G-dwarfs observed with Kepler (Maehara et al. 2015) and with TESS (Tu et al. 2020).

Fig. 14 shows the comparison of E - τ relations for solar flares and stellar flares on various types of stars. Each E - τ relation shows positive correlation and the power-law slope for these E - τ relations are roughly the same: $\tau_{\text{flare}} \propto E_{\text{flare}}^{1/3}$. Maehara et al. (2015) proposed that, if we assume the duration of white-light flare (τ_{flare}) is determined by the reconnection time (τ_{rec}) and the flare energy (E_{flare}) correlates with the magnetic energy stored near the starspots ($E_{\text{mag}} \sim B^2 L^3 / 8\pi$), the correlation between the flare duration and flare energy can be written by the following form,

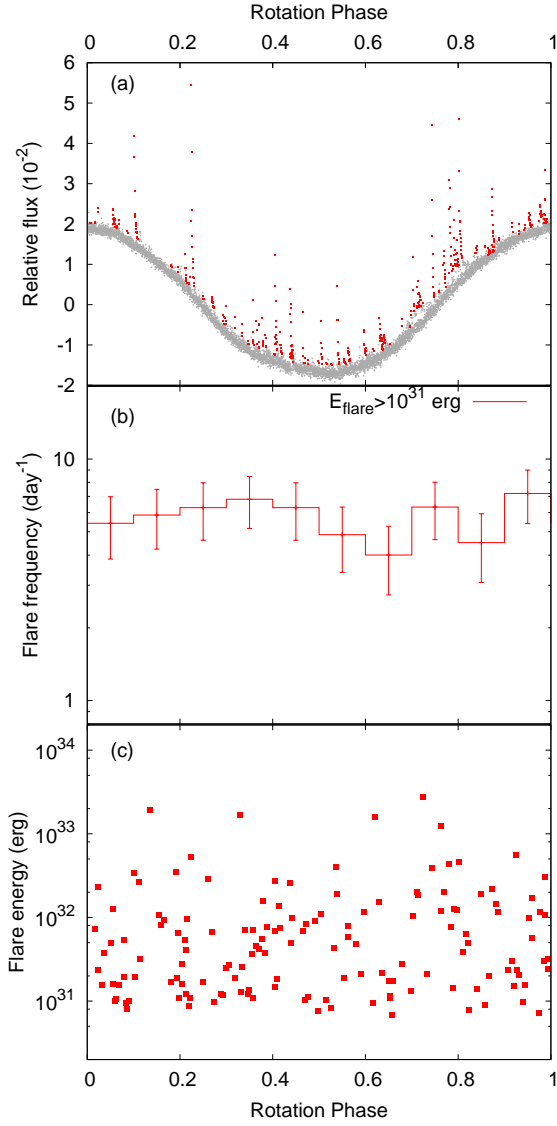


Fig. 12. (a) Phase-folded light curve of rotational brightness variations observed with TESS. The rotation phase was calculated from equation (6). Red dots indicate the data points which are identified as flares. (b) Frequency of flares with the bolometric energy larger than 10^{31} erg as a function of rotation phase. Error bars indicate the square-root of the number of flares in each phase bin. (c) Bolometric energy of each flare as a function of rotation phase.

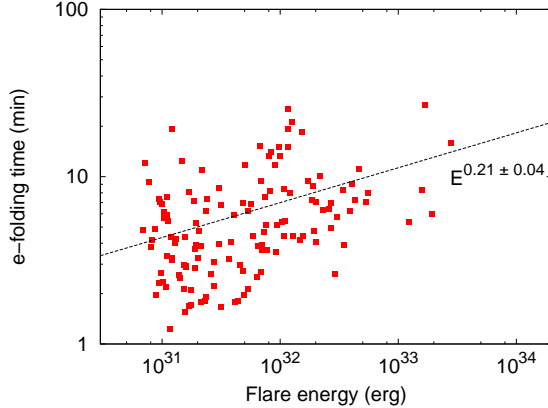


Fig. 13. Scatter plot of flare duration (vertical axis) as a function of the bolometric flare energy (horizontal axis). We used e -folding time from the flare peak time as the duration of flares. The bolometric flare energy was estimated from the TESS light curve under the assumption that the spectral energy distribution of flare component can be represented by the black body radiation with the temperature of 10^4 K.

$$\tau_{\text{flare}} \sim \tau_{\text{rec}} \propto \tau_A/M_A \sim L/v_A/M_A \propto E^{1/3}/B^{2/3}/v_A/M_A, \quad (9)$$

where L , B , v_A , and M_A are the scale length of flaring region, magnetic field strength, Alfvén velocity, and the dimensionless reconnection rate, which ranges from 0.01 to 0.1 in the case of the Petschek-type fast reconnection (Shibata & Magara 2011). This suggests that the power-law slope for the correlation between the duration of flares and flare energy is $\sim 1/3$ if we assume that B , v_A and M_A are roughly the same for flares on different stars.

However, we can see the discrepancy between the duration of solar flares and those of flares on an M dwarf YZ CMi, G-dwarfs, and a giant KIC 2852961: the duration of solar flares and those of flares on YZ CMi and KIC 2852961 are roughly 3 times longer than that expected from the τ - E relation for superflares on G-dwarfs. Chang et al. (2015) and Howard et al. (2019) found the discrepancy between the τ - E relations for M dwarfs with different temperature. Namekata et al. (2017) pointed out the discrepancy between the E - τ relations for solar white-light flares and superflares on G-dwarfs. They proposed the extended scaling-law, which takes into account the dependence on Alfvén velocity ($v_A = B/\sqrt{4\pi\rho}$) as follows:

$$\tau_{\text{flare}} \propto E^{1/3} B^{-5/3} \rho^{1/2}, \quad (10)$$

where ρ is the pre-flare coronal density around the reconnection region. By assuming the constant pre-flare coronal density, equation (10) can give the following new scaling-law:

$$\tau_{\text{flare}} \propto E^{1/3} B^{-5/3}. \quad (11)$$

Since $E \propto B^2 L^3$ (e.g., Shibata et al. 2013), the scaling-law can also be written as

$$\tau_{\text{flare}} \propto E^{-1/2} L^{5/2}. \quad (12)$$

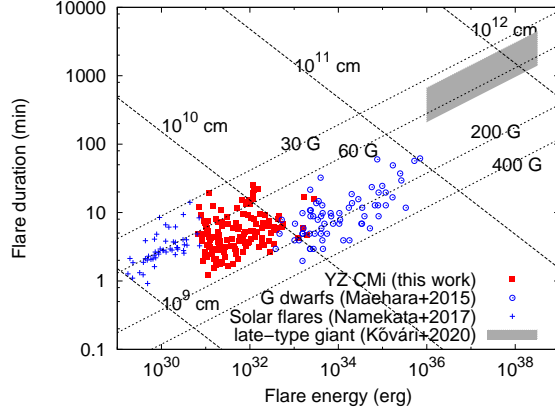


Fig. 14. Comparison of τ - E relations for solar white-light flares (blue crosses; Namekata et al. 2017), stellar flares on an M dwarf YZ CMi (red filled-squares; this work), superflares on solar-type stars (blue open-circles; Maehara et al. 2015), and superflares on a late-type giant KIC 2852961 (gray area; Kővári et al. 2020). Dashed lines indicate τ - E relation based on equation (11) for $B = 30, 60, 200,$ and 400 G. Dotted lines represent another τ - E relation based on equation (12) for $L = 10^9, 10^{10}, 10^{11},$ and 10^{12} cm.

As shown in Fig. 14, each E - τ relation roughly is on the theoretical scaling-row with the constant B (equation (11)). This suggest that one possible explanation for the discrepancy of E - τ relations for solar flares and stellar flares on various types of stars is the difference in the coronal magnetic field strength. Moreover, another theoretical scaling-row given by the equation (12) implies that the scale length of the flare region for the largest flare on YZ CMi is comparable to the stellar radius ($R_{star} \sim 0.3R_{\odot} \sim 2 \times 10^{10}$ cm for YZ CMi). In the case of superflares on solar-type stars and those on a giant KIC 2852961 (gray), the scale length for the largest flares is also comparable to the stellar radius ($\sim 1R_{\odot}$ for solar-type stars and $\sim 10R_{\odot}$ for KIC 2852961). These upper limits suggest that the flare loop length is roughly the same order of magnitude to the stellar radius. The flare loop length estimated from the correlation between electron temperature and emission measure of solar and stellar flares (Shibata & Yokoyama 1999) is the same order of magnitude as the scale length estimated from τ - E relation based on equation (12).

4.5 Flare duration statistics

According to Veronig et al. (2002), the frequency distribution of solar flares as a function of the flare duration can be represented by a power-law function with the power-law index of -2.9 . The similar plots of the frequency distribution as a function of the flare duration (e -folding time) for the flares on YZ CMi are shown in Fig. 15. We found that the frequency distribution of flares on YZ CMi as a function of the flare duration can also be well represented by a power-law function with the power-law index of -2.8 ± 0.1 . This value is comparable to the power-law

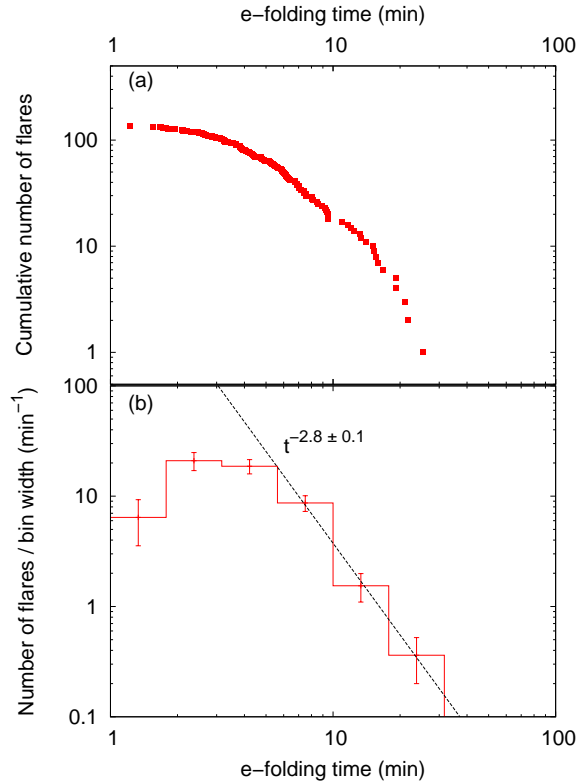


Fig. 15. Number of flares as a function of flare duration. The vertical and horizontal axis indicate the number of flares in each bin and e-folding time of flares.

index for the frequency distribution of solar flares. This similarity in flare frequency distribution as a function of flare duration may come from the similarity in the flare frequency distribution as a function of flare energy and that in the duration-energy correlations for solar flares observed in soft X-rays and for stellar flares observed in optical. The flare frequency distribution as a function of energy (flare fluence) can be well represented by a power-law function ($dN/dE \propto E^\alpha$) with the power-law index of $\alpha = -2.03$ for solar soft X-ray flares (Veronig et al. 2002). In the case of optical flares on YZ CMi, the flare frequency distribution as a function of bolometric energy of flares can also be represented by a power-law function with the power-law index of -1.75 . Moreover, both the duration-energy (flare fluence) correlation ($\tau_{\text{flare}} \propto E_{\text{flare}}^\beta$) for solar soft X-ray flares and that for optical flares on YZ CMi show similar power-law slope ($\sim 1/3$ for solar flares :Veronig et al. 2002; ~ 0.2 for YZ CMi: this work). These similarities between the statistical properties of solar flares and those of stellar flares suggest that the energy release mechanisms are the same for solar and stellar flares.

5 Summary and Conclusions

We carried out time-resolved photometry and spectroscopy of the M-type flare star YZ CMi during the TESS observation window. We detected 4 H α flares from our spectroscopic and photometric observations and one of them exhibited no clear brightening in continuum. The key findings from our observations and are as follows:

1. The H α flares with brightening in continuum tend to have shorter flare duration and larger H β emission line flux than the non-white-light flare.
2. During the non-white-light flare, the blue asymmetry in the H α emission line was observed for ~ 60 min. The line of sight velocity of the blue asymmetry was $-80 - -100$ km s $^{-1}$.
3. If we assume the blue asymmetry in the H α line was caused by a prominence eruption, the mass and kinetic energy of erupted material are estimated to be $10^{16} - 10^{18}$ g and $10^{29.5} - 10^{31.5}$ erg, respectively. Although these values are comparable to those expected from the empirical relations between flare X-ray energy and mass/kinetic energy for stellar events, the estimated kinetic energy is 2 orders of magnitude smaller than that expected from the empirical relation for CMEs on our Sun. This could be understood by the difference between the velocity of prominence eruption and that of CMEs. More simultaneous optical, and X-ray/EUV/radio observations are necessary to fully understand stellar CMEs.
4. The TESS light curve shows rotational modulations with the period of 2.7737 ± 0.0014 d and full-amplitude of 3.6 %. The rotational modulations can also be seen in g - and R_C -band data. The amplitude of the rotational modulations increases as the wavelength decreases (9.8 % in g -band and 7.4 % in R_C -band). These rotational modulations suggest that 10–20 % of the surface of YZ CMi would be covered by starspots.
5. The rotational modulation can also be seen in the equivalent width of H α line during the OISTER observation. The H α line modulation was anti-correlated with rotational modulations in continuum. However, the equivalent width of H α line was almost constant during the APO observation. The TESS light curve suggests that the difference in rotational modulations in H α line between these observations may be caused by the difference in the flare activity during each observation run.
6. The flare frequency and the largest flare energy during the TESS observation period were roughly constant over the rotation phase.
7. The duration of flares (τ) observed with TESS shows a positive correlation with the flare energy. The flare duration distribution shows the power-law distribution ($dN/d\tau \propto \tau^\alpha$) with the power-law index of $\alpha = -2.8 \pm 0.1$, which is consistent with the power-law index of the

flare duration distribution for solar flares.

Acknowledgments

This work was supported by the Optical and Near-infrared Astronomy Inter-University Cooperation Program and the Grants-in-Aid of the Ministry of Education. This work was also supported by MEXT/JSPS KAKENHI Grant Number 17K05400, 20K04032 (H.M.), 18J20048 (K.N.), and 17K14253 (M.Y.). Y.N. was supported by JSPS Overseas Research Fellowship Program. Y.N. also acknowledges the International Space Science Institute and the supported International Team 464: “The Role Of Solar And Stellar Energetic Particles On (Exo)Planetary Habitability (ETERNAL, <http://www.issibern.ch/teams/exoeternal/>)”. This paper includes data collected with the TESS mission, obtained from the MAST data archive at the Space Telescope Science Institute (STScI). Funding for the TESS mission is provided by the NASA Explorer Program. STScI is operated by the Association of Universities for Research in Astronomy, Inc., under NASA contract NAS 526555. In this study, we used the observation data obtained with the Apache Point Observatory (APO) 3.5 m telescope, which is owned and operated by the Astrophysical Research Consortium. We used APO observation time allocated to the University of Washington, and appreciate Suzanne Hawley for helping to plan the observation. We are grateful to APO 3.5m Observing Specialists and other staff members of Apache Point Observatory for their contributions in carrying out our observations. We are grateful to Mr. Isaiah Tristan (University of Colorado Boulder) for valuable suggestions to improve the manuscript. We thank Dr. Jun Takahashi (Nishi-Harima Astronomical Observatory, Center for Astronomy, University of Hyogo) for his support for our observation by using Nayuta Telescope. We also thank Prof. Jeffrey Linsky for useful comments and suggestions that contributed to improve the manuscript.

References

- Airapetian, V. S., Glocer, A., Gronoff, G., et al. 2016, *Nature Geoscience*, 9, 452
- Airapetian, V. S., Barnes, R., Cohen, O., et al. 2020, *International Journal of Astrobiology*, 19, 136
- Allred, J. C., Kowalski, A. F., & Carlsson, M. 2015, *ApJ*, 809, 104
- Alvarado-Gómez, J. D., Drake, J. J., Cohen, O., et al. 2018, *ApJ*, 862, 93
- Alvarado-Gómez, J. D., Drake, J. J., Frascchetti, F., et al. 2020, *ApJ*, 895, 47
- Argiroffi, C., Reale, F., Drake, J. J., et al. 2019, *Nature Astronomy*, 3, 742
- Aschwanden, M. J., Tarbell, T. D., Nightingale, R. W., et al. 2000, *ApJ*, 535, 1047
- Aschwanden, M. J., Caspi, A., Cohen, C. M. S., et al. 2017, *ApJ*, 836, 17
- Audard, M., Güdel, M., Drake, J. J., et al. 2000, *ApJ*, 541, 396
- Baroch, D., Morales, J. C., Ribas, I., et al. 2020, *A&A*, 641, A69
- Benz, A. O., & Güdel, M. 2010, *ARA&A*, 48, 241
- Berdyugina, S. V. 2005, *Living Reviews in Solar Physics*, 2, 8
- Berlicki, A. 2007, *The Physics of Chromospheric Plasmas*, 387
- Bessell, M. S. 2005, *ARA&A*, 43, 293
- Canfield, R. C., Penn, M. J., Wulser, J.-P., et al. 1990, *ApJ*, 363, 318

Canfield, R. C., Reardon, K. P., Leka, K. D., et al. 1996, *ApJ*, 464, 1016

Carlsson, M. & Stein, R. F. 1997, *ApJ*, 481, 500

Chang, S.-W., Byun, Y.-I., & Hartman, J. D. 2015, *ApJ*, 814, 35

Claret, A. 2000, *A&A*, 363, 1081

Claret, A., Hauschildt, P. H., & Witte, S. 2012, *A&A*, 546, A14

Collier Cameron, A., & Robinson, R. D. 1989, *MNRAS*, 236, 57

Collins, K. A., Kielkopf, J. F., Stassun, K. G., et al. 2017, *AJ*, 153, 77

Cranmer, S. R. 2017, *ApJ*, 840, 114

Crosby, N. B., Aschwanden, M. J., & Dennis, B. R. 1993, *Sol. Phys.*, 143, 275

Crosley, M. K. & Osten, R. A. 2018, *ApJ*, 856, 39

Davenport, J. R. A., Hebb, L., & Hawley, S. L. 2015, *ApJ*, 806, 212

Dennis, B. R. & Zarro, D. M. 1993, *Sol. Phys.*, 146, 177

Doyle, L., Ramsay, G., & Doyle, J. G. 2020, *MNRAS*, 494, 3596

Drake, S. A., & Ulrich, R. K. 1980, *ApJS*, 42, 351

Drake, J. J., Cohen, O., Garraffo, C., et al. 2016, *Solar and Stellar Flares and Their Effects on Planets*, 196

Dunstone, N. J., Collier Cameron, A., Barnes, J. R., et al. 2006, *MNRAS*, 373, 1308

Emslie, A. G., Dennis, B. R., Shih, A. Y., et al. 2012, *ApJ*, 759, 71

Fausnaugh, M. M., Burke, C. J., Caldwell, D. A., et al. 2019, *TESS Data Release Notes: Sector 7, DR9*

Fisher, G. H., Canfield, R. C., & McClymont, A. N. 1985, *ApJ*, 289, 414

Fisher, G. H. 1989, *ApJ*, 346, 1019

Fuhrmeister, B., Liefke, C., Schmitt, J. H. M. M., et al. 2008, *A&A*, 487, 293

Fuhrmeister, B., Czesla, S., Schmitt, J. H. M. M., et al. 2018, *A&A*, 615, A14

Fukugita, M., Ichikawa, T., Gunn, J. E., et al. 1996, *AJ*, 111, 1748

Gaia Collaboration, Brown, A. G. A., Vallenari, A., et al. 2018, *A&A*, 616, A1

Gaidos, E., & Mann, A. W. 2014, *ApJ*, 791, 54

Gershberg, R. E. 1972, *Ap&SS*, 19, 75

Gershberg, R. E. 2005, *Solar-Type Activity in Main-Sequence Stars* (Springer: Berlin)

Gilbert, H. R., Holzer, T. E., & MacQueen, R. M. 2005, *ApJ*, 618, 524

Gopalswamy, N., Shimojo, M., Lu, W., et al. 2003, *ApJ*, 586, 562

Gopalswamy, N. 2015, *Solar Prominences*, 381

Graham, D. R., Cauzzi, G., Zangrilli, L., et al. 2020, *ApJ*, 895, 6

Grindlay, J., & Heise, J. 1975, *International Cosmic Ray Conference*, 154

Guedel, M., Benz, A. O., Schmitt, J. H. M. M., et al. 1996, *ApJ*, 471, 1002

Gunn, A. G., Doyle, J. G., Mathioudakis, M., et al. 1994, *A&A*, 285, 489

Hawley, S. L. & Pettersen, B. R. 1991, *ApJ*, 378, 725

Hawley, S. L., & Fisher, G. H. 1992, *ApJS*, 78, 565

Hawley, S. L., Fisher, G. H., Simon, T., et al. 1995, *ApJ*, 453, 464

Hawley, S. L., Allred, J. C., Johns-Krull, C. M., et al. 2003, *ApJ*, 597, 535

Hawley, S. L., Davenport, J. R. A., Kowalski, A. F., et al. 2014, *ApJ*, 797, 121

Heinzel, P., Gouttebroze, P., & Vial, J.-C. 1994, *A&A*, 292, 656

Heinzel, P., Karlicky, M., Kotrc, P., et al. 1994, *Sol. Phys.*, 152, 393

Heinzel, P., Schmieder, B., Fárník, F., et al. 2008, *ApJ*, 686, 1383

Hilton, E. J. 2011, Ph.D. Thesis

Houdebine, E. R., Foing, B. H., & Rodono, M. 1990, *A&A*, 238, 249

Houdebine, E. R., Foing, B. H., Doyle, J. G., et al. 1993, *A&A*, 274, 245

Houdebine, E. R., Mullan, D. J., Paletou, F., et al. 2016, *ApJ*, 822, 97

Honda, S., Notsu, Y., Namekata, K., et al. 2018, *PASJ*, 70, 62

Howard, W. S., Corbett, H., Law, N. M., et al. 2019, *ApJ*, 881, 9

Huang, N., Xu, Y., Sadykov, V. M., et al. 2019, *ApJL*, 878, L15

Ichimoto, K., & Kurokawa, H. 1984, *Sol. Phys.*, 93, 105

Jin, M., Cheung, M. C. M., DeRosa, M. L., et al. 2020, arXiv e-prints, arXiv:2002.06249

Johns-Krull, C. M. & Valenti, J. A. 2000, *Stellar Clusters and Associations: Convection, Rotation, and Dynamos*, 198, 371

Kawabata, K. S., Nagaie, O., Chiyonobu, S., et al. 2008, *Proc. SPIE*, 70144L

Kerr, G. S., & Fletcher, L. 2014, *ApJ*, 783, 98

Kleint, L., Heinzel, P., Judge, P., et al. 2016, *ApJ*, 816, 88

Kotani, T., Kawai, N., Yanagisawa, K., et al. 2005, *Nuovo Cimento C Geophysics Space Physics C*, 28, 755

Kowalski, A. F., Hawley, S. L., Holtzman, J. A., et al. 2010, *ApJL*, 714, L98

Kowalski, A. F., Hawley, S. L., Wisniewski, J. P., et al. 2013, *ApJS*, 207, 15

Kowalski, A. F., Allred, J. C., Daw, A., et al. 2017, *ApJ*, 836, 12

Kowalski, A. F., Wisniewski, J. P., Hawley, S. L., et al. 2019, *ApJ*, 871, 167

Kuridze, D., Mathioudakis, M., Simões, P. J. A., et al. 2015, *ApJ*, 813, 125

Kuridze, D., Mathioudakis, M., Christian, D. J., et al. 2016, *ApJ*, 832, 147

Lacy, C. H., Moffett, T. J., & Evans, D. S. 1976, *ApJS*, 30, 85

Lammer, H., Lichtenegger, H. I. M., Kulikov, Y. N., et al. 2007, *Astrobiology*, 7, 185

Landi, E., & Reale, F. 2013, *ApJ*, 772, 71

Li, Y., Ding, M. D., Hong, J., et al. 2019, *ApJ*, 879, 30

Linsky, J. 2019, *Lecture Notes in Physics*, Berlin Springer Verlag

Lovell, B. 1969, *Nature*, 222, 1126

Kóvári, Z., Oláh, K., Günther, M. N., et al. 2020, *A&A*, 641, A83

Moschou, S.-P., Drake, J. J., Cohen, O., et al. 2019, *ApJ*, 877, 105

Maehara, H., Shibayama, T., Notsu, S., et al. 2012, *Nature*, 485, 478

Maehara, H., Shibayama, T., Notsu, Y., et al. 2015, *Earth, Planets, and Space*, 67, 59

Mitra-Kraev, U., Harra, L. K., Güdel, M., et al. 2005, *A&A*, 431, 679

Morin, J., Donati, J.-F., Petit, P., et al. 2008, *MNRAS*, 390, 567

Muheki, P., Guenther, E. W., Mutabazi, T., et al. 2020, *A&A*, 637, A13

Mullan, D. J. & Paudel, R. R. 2019, *ApJ*, 873, 1

Namekata, K., Sakaue, T., Watanabe, K., et al. 2017, *ApJ*, 851, 91

Namekata, K., Davenport, J. R. A., Morris, B. M., et al. 2020, *ApJ*, 891, 103

Namekata, K., Maehara, H., Sasaki, R., et al. 2020, *PASJ*, doi:10.1093/pasj/psaa051

Neupert, W. M. 1968, *ApJL*, 153, L59

Newton, E. R., Charbonneau, D., Irwin, J., et al. 2015, *ApJ*, 800, 85

Notsu, Y., Honda, S., Maehara, H., et al. 2015, *PASJ*, 67, 33

Notsu, Y., Maehara, H., Honda, S., et al. 2019, *ApJ*, 876, 58

Odert, P., Leitzinger, M., Hanslmeier, A., et al. 2017, *MNRAS*, 472, 876

Odert, P., Leitzinger, M., Guenther, E. W., et al. 2020, *MNRAS*, 494, 3766

Osten, R. A., & Wolk, S. J. 2015, *ApJ*, 809, 79

Ozaki, S., & Tokimasa, N. 2005, *Ann. Rep. Nishi-Harima Astron. Obs.*, 15, 15

Pettersen, B. R., Kern, G. A., & Evans, D. S. 1983, *A&A*, 123, 184

Reid, I. N., & Hawley, S. L. 2005, *New Light on Dark Stars Red Dwarfs* (Chichester: Praxis Publishing)

Reiners, A. & Basri, G. 2007, *ApJ*, 656, 1121

Reiners, A. & Basri, G. 2009, *A&A*, 496, 787

Ricker, G. R., Winn, J. N., Vanderspek, R., et al. 2015, *Journal of Astronomical Telescopes, Instruments, and Systems*, 1, 014003

Segura, A., Walkowicz, L. M., Meadows, V., et al. 2010, *Astrobiology*, 10, 751

Shakhovskaia, N. I. 1989, *Sol. Phys.*, 121, 375

Schmieder, B., Forbes, T. G., Malherbe, J. M., et al. 1987, *ApJ*, 317, 956

Schrijver, C. J., Cote, J., Zwaan, C., et al. 1989, *ApJ*, 337, 964

Schrijver, C. J. 2020, *ApJ*, 890, 121

Scheucher, M., Grenfell, J. L., Wunderlich, F., et al. 2018, *ApJ*, 863, 6

Shibata, K., & Yokoyama, T. 1999, *ApJL*, 526, L49

Shibata, K., & Yokoyama, T. 2002, *ApJ*, 577, 422

Shibata, K., & Magara, T. 2011, *Living Reviews in Solar Physics*, 8, 6

Shibata, K., Isobe, H., Hillier, A., et al. 2013, *PASJ*, 65, 49

Shibayama, T., Maehara, H., Notsu, S., et al. 2013, *ApJS*, 209, 5

Shoji, M., & Kurokawa, H. 1995, *PASJ*, 47, 239

Silverberg, S. M., Kowalski, A. F., Davenport, J. R. A., et al. 2016, *ApJ*, 829, 129

Soubiran, C., Jasniewicz, G., Chemin, L., et al. 2018, *A&A*, 616, A7

Spangler, S. R., Shawhan, S. D., & Rankin, J. M. 1974, *ApJL*, 190, L129

Stellingwerf, R. F. 1978, *ApJ*, 224, 953

Strassmeier, K. G. 2009, *A&AR*, 17, 251

Švestka, Z., Kopecký, M., & Blaha, M. 1962, *Bulletin of the Astronomical Institutes of Czechoslovakia*, 13, 37

Takasao, S., Mitsuishi, I., Shimura, T., et al. 2020, arXiv:2008.04255

Tei, A., Sakaue, T., Okamoto, T. J., et al. 2018, *PASJ*, 70, 100

Tilley, M. A., Segura, A., Meadows, V., et al. 2019, *Astrobiology*, 19, 64

Tu, Z.-L., Yang, M., Zhang, Z. J., et al. 2020, *ApJ*, 890, 46

van Maanen, A. 1945, *PASP*, 57, 216

Veronig, A., Temmer, M., Hanslmeier, A., et al. 2002, *A&A*, 382, 1070

Vida, K., Kriskovics, L., Oláh, K., et al. 2016, *A&A*, 590, A11

Vida, K., Leitzinger, M., Kriskovics, L., et al. 2019, *A&A*, 623, A49

Vanderspek, R., Doty, J., Fausnaugh, M., et al. 2018, *TESS Instrument Handbook*, Tech. rep., Kavli Institute for Astrophysics and Space Science, Massachusetts Institute of Technology

Wang, S.-i., Hildebrand, R. H., Hobbs, L. M., et al. 2003, *Proc. SPIE*, 1145

Warren, H. P. 2006, *ApJ*, 637, 522

Watanabe, K., Shimizu, T., Masuda, S., et al. 2013, *ApJ*, 776, 123

Watanabe, K., Kitagawa, J., & Masuda, S. 2017, *ApJ*, 850, 204

Yamashiki, Y. A., Maehara, H., Airapetian, V., et al. 2019, *ApJ*, 881, 114

Yashiro, S., & Gopalswamy, N. 2009, *Universal Heliophysical Processes*, 233

Zboril, M. 2003, *Astronomische Nachrichten*, 324, 527